



UNIVERSITY OF GRONINGEN

BACHELOR PROJECT

# Water in Protoplanetary Disks

*Jelle Bor*

supervised by  
Dr. Inga KAMP



# Abstract

The aim of this research is to gain a better insight in the water distribution within protoplanetary disks. Water is an important molecule in these disks and is interesting for planet formation. In this study, water column densities have been calculated as function of distance from the star for several models with different parameters, by using the ProDiMo code. Subsequently fits were made to these surface density profiles used to investigate possible correlations between the parameters and the radial water column density profile.

The snow line, the point at which water freezes out, can be obtained from these models too. By relating the snow line to the changing parameters, the gas mass and flaring parameter of the disk turn out to affect the position of the snow line.

Also the water emission lines are extracted from the code and are related to the parameters resulting in again several correlations. The position of the snow line depends on the gas mass and the flaring. When searching for a relation between the emission line ratios of some prominent lines and the position of the snow line, a tentative relation is found.



# Contents

<b>Abstract</b>	<b>3</b>
<b>1 Introduction</b>	<b>7</b>
<b>2 The Model</b>	<b>13</b>
2.1 The ProDiMo code . . . . .	13
2.2 From Abundances to Column Densities . . . . .	15
2.3 The Column Density of Water . . . . .	15
2.3.1 The Snow-line . . . . .	16
2.3.2 Fitting the water profile . . . . .	18
2.3.3 Mass accumulation and the accuracy of fitting . . . . .	20
<b>3 The Water Profile</b>	<b>23</b>
3.1 Dust-to-gas mass ratio . . . . .	23
3.2 Settling . . . . .	25
3.3 Structure of the disk . . . . .	27
3.4 Dust grain sizes and size distributions . . . . .	28
3.5 The Interstellar medium UV radiation field . . . . .	29
3.6 PAHs in disks . . . . .	30
3.7 Gas masses . . . . .	31
3.8 $\alpha$ and the Snow region . . . . .	32
<b>4 Water Emission Lines</b>	<b>36</b>
4.1 Ortho- and Para-water . . . . .	36
4.2 Water lines . . . . .	37
4.3 Changing parameters and emission . . . . .	41
4.3.1 Small changing 17.22 line . . . . .	42
4.3.2 Large changing 17.22 line . . . . .	44
4.4 The Snow line and emission lines . . . . .	50
<b>5 Conclusion and Discussion</b>	<b>53</b>
<b>6 Appendix</b>	<b>58</b>
<b>Bibliography</b>	<b>63</b>



# Chapter 1

## Introduction

In this chapter first the general field of protoplanetary disks will be introduced, before discussing the main purpose of this research.

During the process of star formation, the interstellar medium gravitationally collapses to form a star. Around this star a (rotating) disk of material is formed called the protoplanetary disk. From this disk smaller astronomical objects can form, such as planets. Real images of protoplanetary disks are shown in figure 1.1. and 1.2, however these kind of pictures are rare. Figure 1.3 shows a schematic drawing of a protoplanetary disk to illustrate how such an object can be interpreted. The interstellar medium consists mainly out of gas but contains dust grains as well (approx. 1 % of the total mass). However, the amount of dust can vary between environments as dust has the possibility to grow and decouple from the gas, which is visible in protoplanetary disks.

Since a protoplanetary disk consists of gas and dust it is of great importance to study those components in order to understand the processes at work. Gas and dust can both make the disk optically thick and therefore cause that emission lines (light) cannot escape from within those regions. Therefore we can only see light passing through from optically thin regions (figure 1.3).

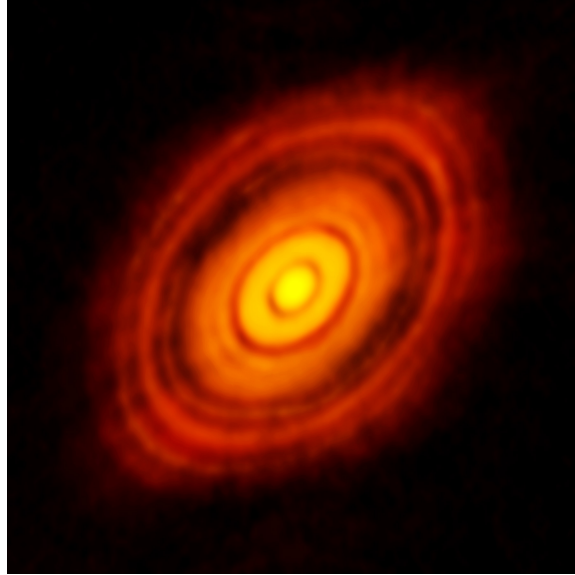


Figure 1.1: The young star HL Tau and its protoplanetary disk [1].

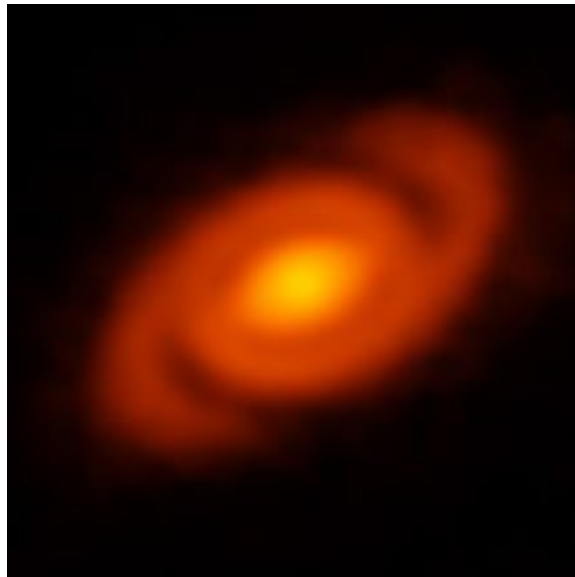


Figure 1.2: A protoplanetary disk surrounding the young star Elias 2-27 [2].

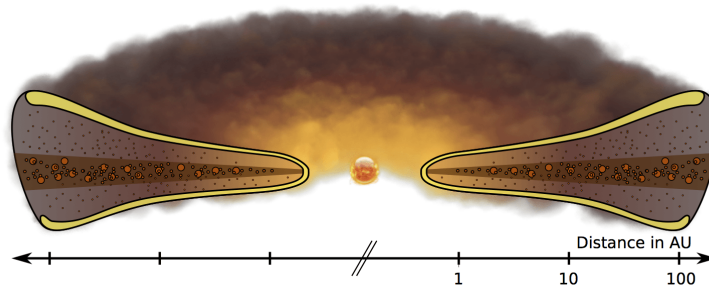


Figure 1.3: Schematic image of a protoplanetary disk[6]. In the middle sits a host star which is surrounded by the disk. The dust grains are shown in the disk and they are surrounded by the gas. The larger dust particles are concentrated near the disk midplane, while the small grains remain well-mixed vertically. The yellow regions indicate the optically thin regions, which contain less gas and dust.

Different gaseous chemical species react with each other in equilibrium or freeze out when the temperature is low enough. As there are many kinds of species and reactions, this is already very complicated. On top of this the detection of gas is more challenging than dust. The emission of gas is in discrete lines and bands, while dust contributes to continuum emission. Therefore the detection of gas requires a high spectral resolution and their emission bands can only be detected when the gas temperatures are higher than the dust temperatures. Dust grains in protoplanetary disks, can have different sizes and are subject to competitive processes occurring in the disk, such as depletion, settling, mixing (of small and big grains) and encounters (leading to growth or fragmentations) all depending on size.

Generally speaking one can say that, the bigger the dust grains within a disk are, the older the disk is, however this does not necessarily have to be true. As turns out the submm continuum slope of a spectral energy distribution (SED), of a protoplanetary disk, can usually be described by a power law which indicates a grain size distribution with a certain maximum grain size. On dust grains (figure 1.5), which are assumed to be a mixture of silicates and carbon compounds, also several interesting processes happen. In this thesis ice, which sticks to the grains, will be the main subject under study. Processes that occur on icy grains are schematically shown in figure 1.4.

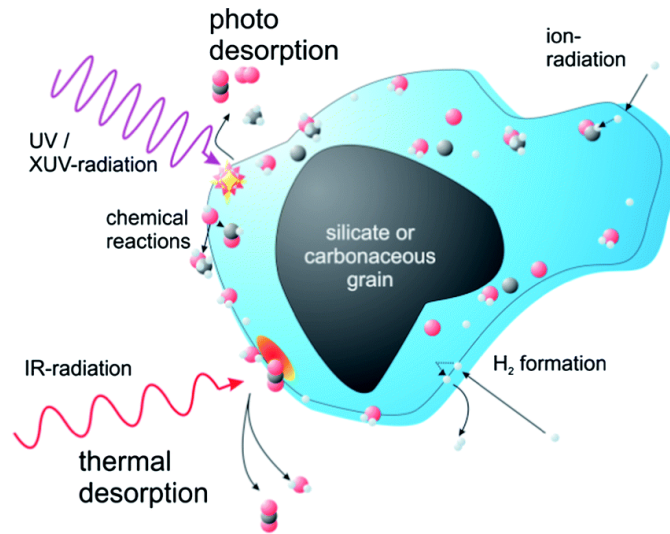


Figure 1.4: The physical processes that take place on icy grains [5].

Within protoplanetary disks there are also so called polycyclic aromatic hydrocarbons (PAH's) present which contribute to the total opacity function of the disk as well. PAHs are of major importance to the gas physics in the disk, as they are an important source of heating within the irradiated layers. Such a molecule is shown in figure 1.6.

The neighborhood of a protoplanetary disk can also influence the reactions occurring in the disk. External light can interact with the gas and ionize species either by the host star itself or by the surrounding astronomical neighborhood, radiating very energetically in the ultraviolet spectrum. The defined solar neighborhood integrated flux is  $G_0 = 1.6 \times 10^{-3} \text{ erg s}^{-1} \text{ cm}^{-2}$  and is used as a standard measure.

Lastly the structure of the disk is of importance too. In figure 1.5 several protoplanetary disks are shown which all are flaring, but this does not have to be necessarily the case. Flaring is that the outer disk is geometrically thicker than the inner disk, this changes the appearance of the disk and therefore the structure since more light is intercepted by the disk when a disk is more flared. The first observational evidence came from the infrared slope in the SED which needed flaring to be explained.

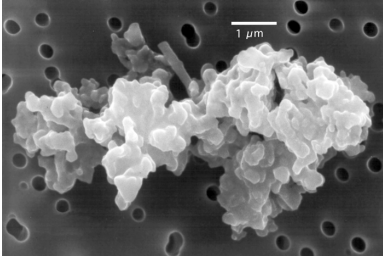


Figure 1.5: Porous chondrite interplanetary dust particle [8].

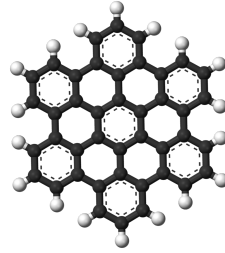


Figure 1.6: Representation of hexabenzocoronene, a PAH, ball-and-stick model showing all carbon and hydrogen atoms [9].

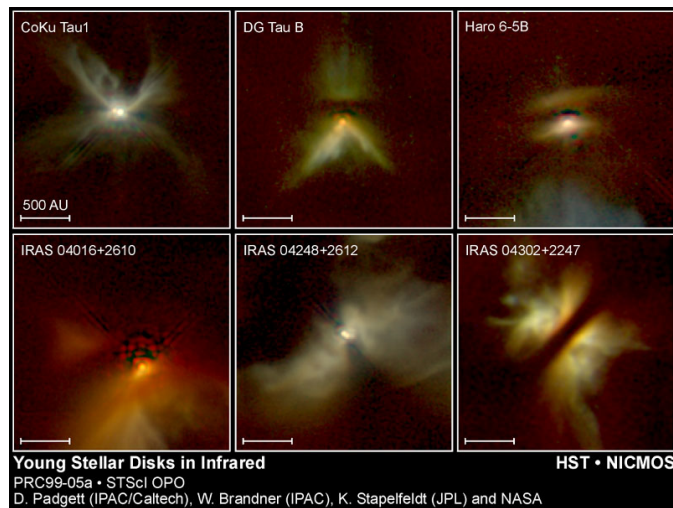


Figure 1.7: Edge-on disks in the Taurus star formation region [7].

All the above described processes together, contribute to the appearance of the disk. As all of the above mentioned processes also contribute to the thermal energy within the disk, the temperature distribution should be a good reflection of the occurring processes. When looking at the temperature distribution of a protoplanetary disk a general image appears. Horizontally, a temperature drop is seen from close to the star to the outer parts of the disk. Vertically this drop is seen from the top layers to the mid-plane.

The protoplanetary disk is of great interest in trying to understand planet formation and the important role of water within this process. Water can be present in the disk in different phases. It is mostly present in gas form (near the star) but also occurs in ice form. The transition point at which icy grains are formed is known as the snow line. This study is about finding out how water is distributed in a protoplanetary disk (for different initial conditions) by making use of a chemical computer model (Woitke et al.(2009)), which describes the disk and takes into account the physical and chemical processes that occur within the disk.

From these models one can derive the water profile of a disk by extracting column densities. The found profiles will be compared to analytical profiles from previous research. However, this can be taken one step further. By extracting the water emission lines from the different models they can be compared and used to search for a relation between the emission spectrum and the position of the snow line. Zhang et al.(2013) presented an observational reconstruction of the radial water vapor content at the surface of the TW Hya protoplanetary disk and reported the first localization of the snow line. They fitted a two-dimensional disk model to the available star and disk photometry from the Spitzer and Herschel telescopes of all observed  $H_2O$  lines, using a simple step function parameterization of the water vapor content near the disk surface. This is very promising research and this thesis is set out to test these ideas with the ProDiMo models. Their shortcomings could be oversimplified assumptions, that is the use of a simple step function and/or their lack of detailed chemistry in their model.

## Chapter 2

# The Model

In this section the output of the code will be discussed and the methodology to obtain the water profile of a protoplanetary disk.

### 2.1 The ProDiMo code

The ProDiMo code (shorthand for Protoplanetary Disk Model) is the complex code used to determine the water profile of a protoplanetary disk. It returns large amounts of data. All the chemical abundances of different species at different locations will be returned, taking into account physical processes such as photo-ionization (by the central star) and chemical process such as interaction between species (leading to formation and destruction) and freeze-out processes. The interesting part of this is to observe what changes occur in the model, and hence the water distribution in the disk, when changing a parameter over a certain range. This will be further discussed in chapter 3.

An example of an output of the code is shown in figure 2.1. This figure shows the water abundance as the color ( $\varepsilon(H_2O)$ ) in the disk as a function of radius ( $r$ ) and relative height ( $z/r$ ). This is like looking edge on to the disk. In figure 2.1 two dashed lines indicate the extremes in temperature differences. The temperature within the disk decreases rapidly moving away from the star due to the fact that the radiation from the star cannot penetrate very deeply into the disk. This results in less ionization of species (less heating) and thus lower temperatures.

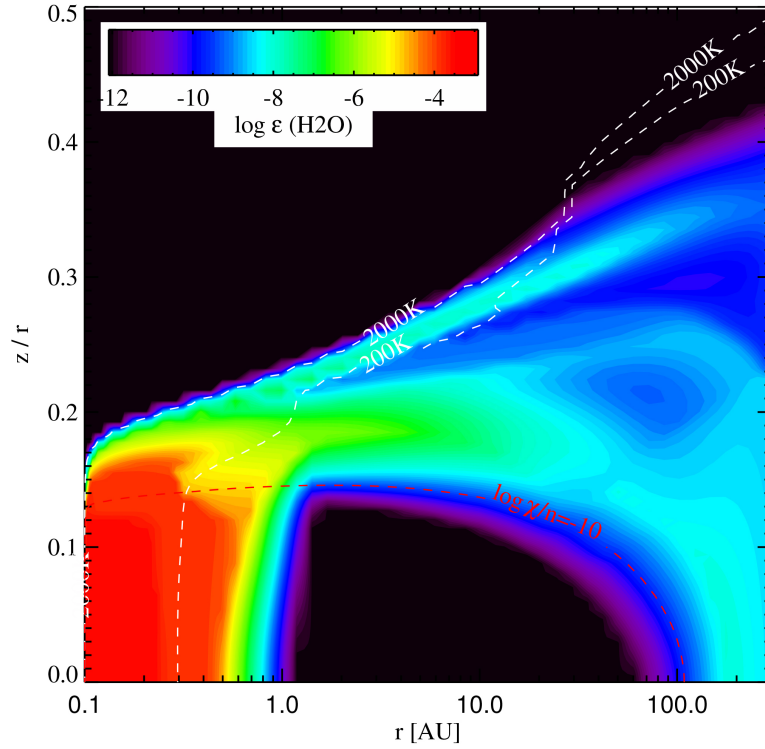


Figure 2.1: Example of the ProDiMo of code water abundances of the  $a_{max} = 250\mu\text{m}$  model.

In figure 2.1 a black region in the middle of the disk is visible starting at a radius of  $\sim 1$  AU and ending at  $\sim 100$  AU. In this box almost no water is present in gas form. However ice is being formed in this part of the disk because it is cold there (see above for reasoning behind the temperature drop). The sudden drop (vertical line at  $\sim 1$  AU) is the indication that there will be no significant amounts of water vapor anymore, however ice dominates (by increasing radius). This region where water changes its phase is very interesting, because the amount of water present is of fundamental importance to planet formation. A common concept used when dealing with these phase transitions of water is the snow line. The snow line is the line that describes the transition between water in gas phase to ice. The snow line is not a set definition but more of a vague concept. This subject will be discussed in more detail further on in this chapter.

## 2.2 From Abundances to Column Densities

At every position in the disk the hydrogen density follows from the code, which is the sum of all the hydrogen present, i.e.  $n_{<H>} = n(H) + 2 \cdot n(H_2)$  [ $\text{cm}^{-3}$ ], where  $n$  is the number density. The abundance of  $H_2O$  is related to the number density as follows  $\varepsilon_{H_2O} = n_{H_2O} / n_{<H>}$ . The total column density at a position  $r$  can then be calculated by integrating from 0 to the height in the disk  $z_{max}$ . This results in equation 2.1 for calculating the total hydrogen column density for the top half of the disk:

$$N_{<H>} = \int_0^{z_{max}} n_{<H>}(z) dz \quad [\text{cm}^{-2}] \quad (2.1)$$

However, the total column density of water is searched for. By using the relations described above, equation 2.2 can be determined to calculate the water column density:

$$N_{H_2O} = \int_0^{z_{max}} n_{<H>}(z) \cdot \varepsilon_{H_2O}(z) dz \quad [\text{cm}^{-2}] \quad (2.2)$$

## 2.3 The Column Density of Water

Now that a method to calculate the column density of water in gas phase has been obtained (or actually any species in the disk when it is multiplied with different abundances), this can be plotted in order to understand what happens with the water in the disk. The data from the model in figure 2.1 have been used to calculate the water column densities which results in figure 2.2.

In figure 2.2 three lines are visible. First, the total gas column density is shown (green) to use as comparison. This line is directly generated from the data. Secondly the column density that has been calculated by the method described in the previous section is shown for two species, namely water in gas (blue) and in ice (red) form. This data makes sense, because water dominates in gas form nearby the star. Moving radially outward from the star, more and more water in ice form occurs. The intersection point between those curves has subsequently been calculated. This was done by taking the minimum of the subtraction of the data (water in ice and gas phase) from each other. In figure 2.3 the calculation is graphically shown. This calculation will be used in the next section which discusses the snow line in more detail.

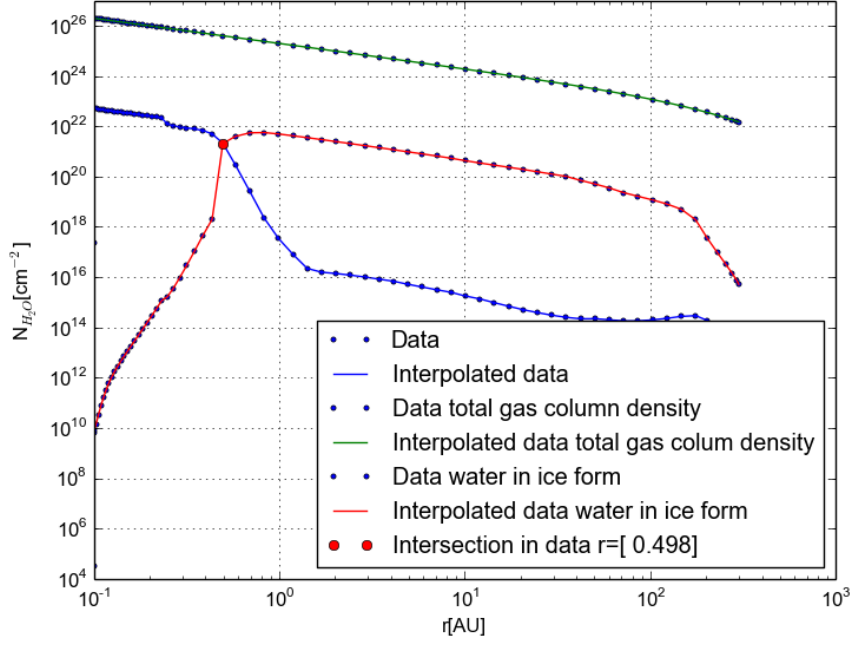


Figure 2.2: Example of the water column densities of the  $a_{max} = 250\mu\text{m}$  model.

### 2.3.1 The Snow-line

The snow line has been mentioned a couple of times in this thesis, but how can it be defined? Currently there is no agreed definition for the snow line, which is used to describe the transition between water in gas and in ice phase. The direct output of the code (as figure 2.1) returned a value for the snow line as the point where the abundances of the water species of gas and ice equaled each other. This is at 0.435 AU for the  $a_{max} = 250\mu\text{m}$  model. The point where the gas and ice are equal in column densities (calculated in the previous section, for the  $a_{max} = 250\mu\text{m}$  model: 0.489 AU) is not necessarily the same (they differ  $\sim 0.05$  AU), but, as should be mentioned, a good starting point to describe the transition.

By looking at figure 2.2 the snow line can now be defined. In order to improve the concept of the snow line a different approach to this problem should be taken rather than treating it as the place the ice abundance takes

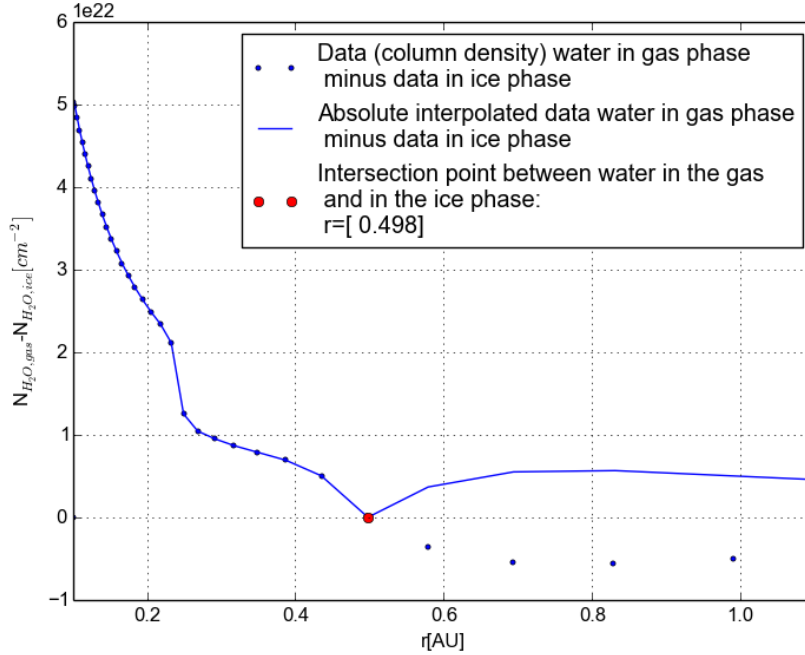


Figure 2.3: Graphical example of the calculation of the intersection between gas and ice column densities of water of the  $a_{max} = 250\mu m$  model.

over from the water abundance. As the area where the transition takes place looks more like a region than a line, a first step would be to treat the area as a snow region rather than a snow line. The next step is to establish boundaries to the snow region. As ice takes over at the calculated point, this should be considered as a reasonable inner limit for the snow line. When following the profile to the outer part of the disk, the water in gas phase decreases more and more. However, at a certain point it flattens out and stays roughly constant. At that point the ice completely dominates the water in the disk. So as a outer limit for the snow region, a good suggestion would be to use the point where the water column density is not decreasing significantly anymore. This point can be considered as a multiplication of the earlier calculated value for the equality between gas and ice column density by a factor  $\alpha$ . Defining  $rm$  to be the intersection of the water in gas and ice column densities, the defined snow region is between  $rm$  and  $\alpha \times rm$ , which often will be referred to as transition region throughout this

thesis. In the example  $\alpha$  was set to be 3, in the appendix of output example data can be found. Now a more quantitative definition for the snow line is formulated, which will be used in the oncoming section.

### 2.3.2 Fitting the water profile

Zhang et al. (2013) conducted research on the snow line in a transitional disk. This means that the disk has a gap due to for example the formation of a planet within the disk. In their paper they propose to fit the water profile as a step function by making use of the snow line. This is equivalent to saying that before the snow line the water abundance has a certain value and after it another value (lower). However in order to obtain a water column density profile one multiplies this function with the total gas column density ( $N_{<gas,tot>}$ ). This idea can be tested with the data found from the ProDiMo code. So before and after  $rm$ , a least squares method is used to find the best fit ( $a$  and  $b$ ) to the data of water in the gas phase. This takes the form of equation 2.3. Note that  $rm$  is a good choice to be the snow line inner limit in this case, because usually the equality of the abundances is at even smaller radii and will fail even more to fit the profile nicely as will be made clear in the next section. Also note that the fitting will be done in semi-logarithmic scale, because that works better for fitting in these cases.

$$\log_{10}(N_{H_2O}) = \begin{cases} a & r \leq rm \\ b & r > rm \end{cases} \cdot N_{<gas,tot>} \quad (2.3)$$

Another interesting idea is to fit the data by analytic functions, but this time consider the idea of the snow region. This is done by using the least squares method as above to fit two linear lines to the left part of the data ( $a$  and  $b$ ) and the right part ( $c$  and  $d$ ) (i.e. from 0 to  $rm$  and from  $\alpha \times rm$  to the outer radius):

$$\log_{10}(N_{H_2O}) = \begin{cases} ar+b & r \leq rm \\ cr+d & r \geq \alpha \times rm \end{cases} \quad (2.4)$$

Then, these two linear graphs are added to each other and another least squares method is used to fit a parameter ( $e$ ), which takes into account the transition region. At small distances from the star ( $r < rm$ ) the first linear fit dominates and at large distances from the star ( $r > rm$ ) the second fit linear fit dominates. This can be represented as:

$$\log_{10}(N_{H_2O}) = \frac{1}{1 + (\frac{r}{e})^4} \times (ar + b) + \frac{1}{1 + (\frac{e}{r})^4} \times (cr + d) \quad (2.5)$$

To combine ideas a 2-step function can be made which makes use of the regime between  $rm$  and  $\alpha \times rm$ . So this function was fitted too with the least squares method and is represented as:

$$\log_{10}(N_{H_2O}) = \begin{cases} a & r \leq rm \\ b & rm < r < \alpha \times rm \\ c & r \geq \alpha \times rm \end{cases} \cdot N_{\langle gas, tot \rangle} \quad (2.6)$$

All these fits were made and plotted in figure 1.4. The figure shows that the proposed function (equation 2.5) fits very well. The 2-step function fits reasonably well, but does not follow the curvature of the water profile at all. The simple step function is similar to the 2-step function but mismatches the simulated data even more in the transition region of the disk. The next section will discuss this in more detail. Parameters of all models to the example data can be found in table 2 of the appendix.

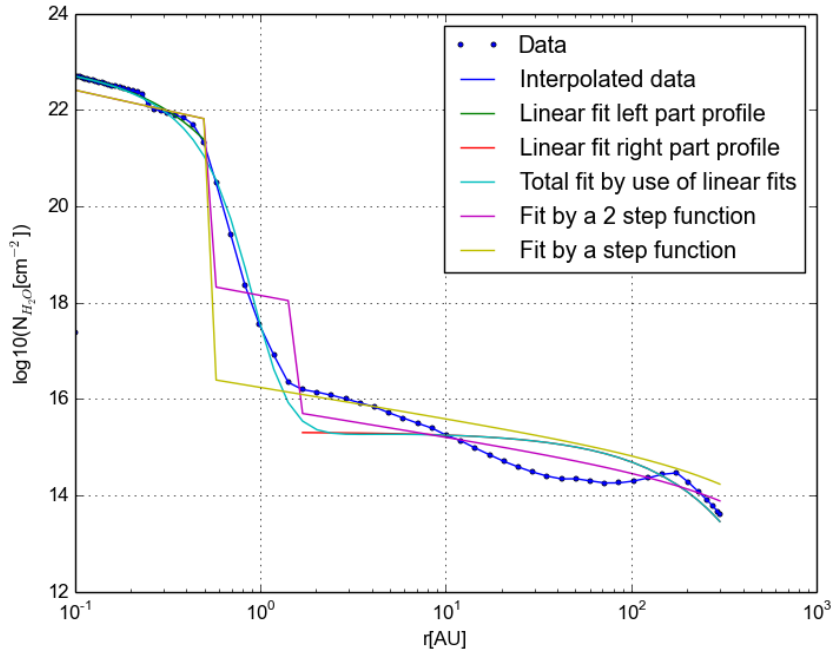


Figure 2.4: Example of fits to a water column density profile of the  $a_{max} = 250\mu\text{m}$  model.

### 2.3.3 Mass accumulation and the accuracy of fitting

Now that multiple water profile fits have been found, it is useful to test which fit works best in reproducing the data. To do so, the total water mass (in gas phase) in the disk can be calculated by integrating the column density (equation 2.7). In this case the simple Simpsons rule has been used. Note that this results in the number of molecules as the unit of the accumulated mass and that the radii in equation 2.7 have to be converted to cm.

$$M_{H_2O}(R) = \int_{r_{in}}^R 2\pi \cdot r \cdot N(r) dr = \sum_i 2\pi r_i \frac{1}{2} (N_i + N_{i+1}) (r_{i+1} - r_i) \quad [\text{n}] \quad (2.7)$$

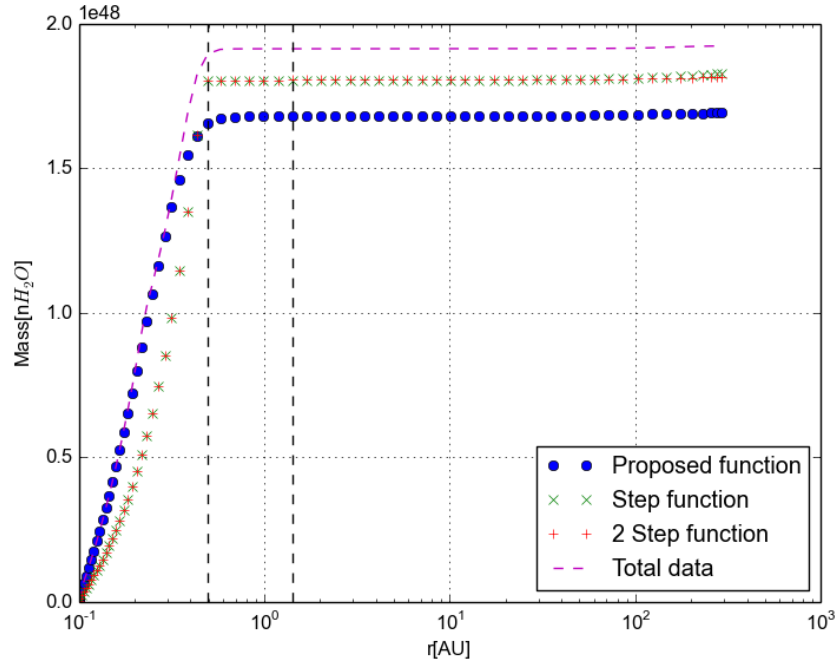


Figure 2.5: Example of cumulative mass function (water is gas phase) of the data and fits of the  $a_{max} = 250\mu\text{m}$  model.  $10^{48}$   $H_2O$  molecules correspond to a mass of  $5 \times 10^{-3} M_{\oplus}$ .

With this formula one can calculate the cumulative mass function ( $M_{H_2O}(R)$ ) in the disk which is represented in figure 2.5. The dashed lines, from left to right, are respectively  $rm$  and  $\alpha \times rm$  and are shown for reference. As one can see the proposed function follows the data well up to a certain point just before  $rm$ , while the step functions do not. After that point, the step functions will be considered constant too. This is due to the fact that while increasing the radial distance, the gas phase water column density decreases approximately a factor  $10^9$ . Therefore the small differences in the outer parts of the disk will not contribute to the total mass. Note that a small deviation in the inner part of the disk will result in a reasonably large deviation in the total mass. This is what happens with the proposed function, nevertheless it has by far the best shape of all considered models.

The important part to fit, as seen in figure 2.4, is the transition region, because here the largest changes happen. Therefore normalizing the data at  $rm$  and plotting up to  $\alpha \times rm$  is a better way to compare the functions. Comparing the proposed function with the step functions would be unfair at this moment because these functions gain a bit more mass just before  $rm$ , which makes them seem better at first glance (figure 2.5). However, when looking at the normalized cumulative mass function (figure 2.6) it becomes clear that the step functions do not fit at all. In this graph, it can clearly be seen that the proposed function is a good fit to the data. The calculated percentages of deviation with respect to the accumulative mass of the data amount to 35% for the proposed function, while the step function deviates 100% and the 2-step function 90% . Note that by calculating the deviation only the last point of the cumulative mass function is of importance.

All in all this shows that the function based on the new interpretation of the snow line is by far the best fit.

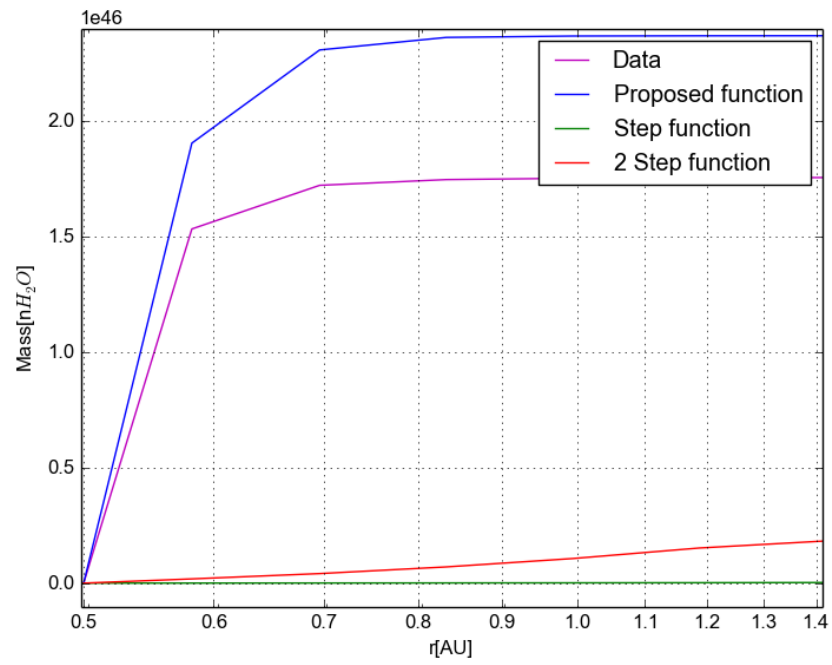


Figure 2.6: Example of normalized accumulated mass in the transition region of the  $a_{max} = 250\mu\text{m}$  model.

## Chapter 3

# The Water Profile

So far it has been discussed how the model works, how water gas phase and ice surface density profiles can be extracted and how it can be interpreted. Different fitting approaches and the idea of the transition region are discussed. One of the aims of this study is to understand what happens when the conditions in the disk are changed and the subsequent effects on the water surface density profile and the snow line. In order to investigate this, a standard disk model is used, the so called monolithic disk model. This model is defined by the properties shown in table 3.1 below. These kinds of disks are typically found around T Tauri (K-type) stars, the stellar properties are also listed in table 3.1. In the next sections the simulations of Antonellini et al. (2015) are post-processed for different parameters to determine their influence on the water profile in the disk. The chosen parameters have been selected because of their role in the protoplanetary disk discussed in the introduction. The important reaction channels that are relevant to water formation and destruction in the standard model, are stated in table 1 of the appendix. All plots are fits of the water column density data by the found function (equation 2.5) to describe the profile in the best way.

### 3.1 Dust-to-gas mass ratio

The dust-to-gas mass ratio can range from hardly containing dust at all, in which case it is then called a Debris disk, to the extreme case of being composed of dust almost entirely. The parameter  $d/g$  represents the dust-to-gas mass ratio and ranges from  $10^{-3}$  up to 100 to reproduce the situations of a dust poor and dust rich disk. Note that the gas mass remains constant.

Central star and radiation field parameters		
Parameter	Symbol	Value
Photospheric temperature	$T_{eff}$ [K]	4400
Stellar mass	$M_*$ [ $M_\odot$ ]	0.8
Stellar Luminosity	$L_*$ [ $L_\odot$ ]	0.7
FUV excess	$L_{UV}/L_*$	0.01
UV powerlaw exponent	$p_{UV}$	0.2
X-ray luminosity	$L_X$ [erg/s]	$10^{30}$
X-ray minimum energy	$E_{min,X}$ [keV]	0.1
X-ray temperature	$T_X$ [K]	$10^7$
Disk parameters of the standard model fixed for all measurements		
Parameter	Symbol	Value
Radial $\times$ vertical grid points	$N_{xx} \times N_{zz}$	$70 \times 70$
Outer radius	$R_{out}$ [AU]	300
Inner radius	$R_{in}$ [AU]	0.1
Surface density power law index	$\epsilon$	1.0
Minimum dust size	$a_{min}$ [ $\mu m$ ]	0.05
Reference radius	$R_0$ [AU]	0.1
Scale height at reference radius	$H_0$ [AU]	$3.5 \times 10^{-3}$
Tapering-off radius	$R_{taper}$ [AU]	200
Chemical heating efficiency	-	0.2
Settling description	-	Dubrulle
Cosmic ray ionization rate	$\zeta_{CRs}$ [ $s^{-1}$ ]	$1.7 \times 10^{-17}$
Distance	d[pc]	140
Turbulence viscosity coefficient	$\alpha_{vis}$	0
Disk inclination	[deg]	30

Table 3.1: Overview of the fixed model parameters for the standard T Tauri model.

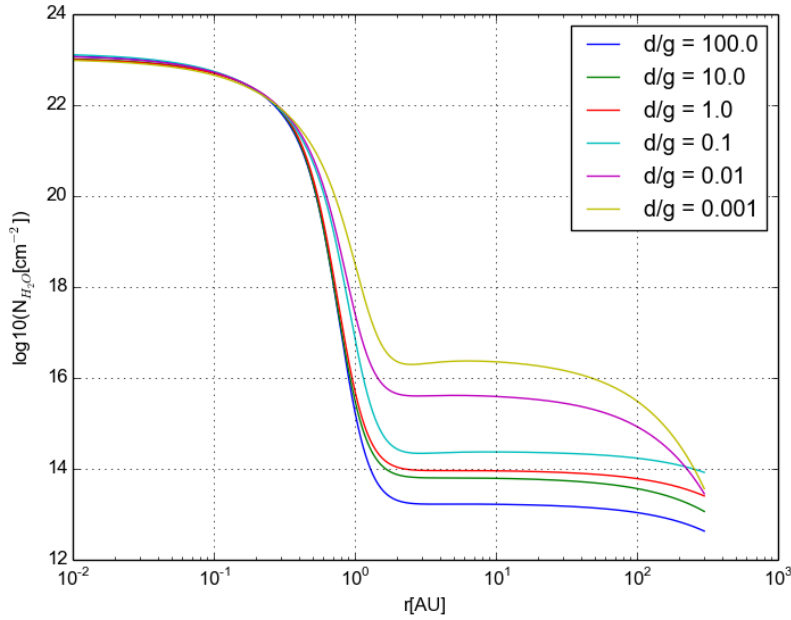


Figure 3.1: The change in parameter  $d/g$  and the resulting water profiles.

Figure 3.1 shows that a higher dust-to-gas mass ratio results in a steeper slope and a lower water column density (gas) in the outer parts of the disk. This can be explained by the following process: When there is more dust in the disk, UV radiation (coming from the host star) can penetrate less deeply into the disk as it is blocked by the dust, the medium is more optically thick. This results in less photo-desorption and subsequently less gas phase water present in the outer parts of the disk. As UV-radiation hits the ice on the dust grain, it can return a water molecule back into the medium (as gas). This process of photo-desorption is shown schematically in figure 1.2.

### 3.2 Settling

Settling has been mentioned as an important parameter in the protoplanetary disk. As it is complicated to accurately describe settling, a simplified approach is used to describe the process as accurate as possible. This is based on the balance between gravity and vertical mechanical gas mixing

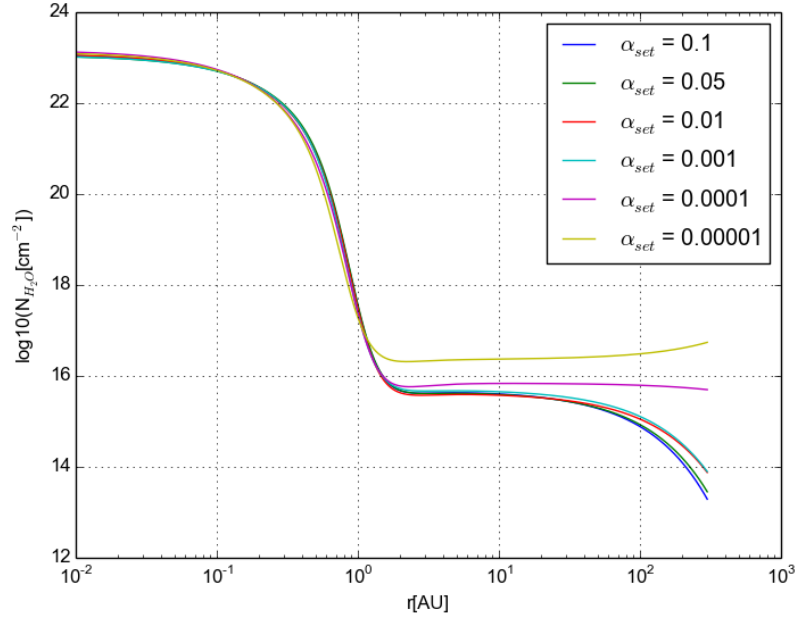


Figure 3.2: The change in parameter  $\alpha_{set}$  and the resulting water profiles.

effects on dust grains. Note that passive disks are modeled in this study which means that no viscous heating or accretion takes place in the disk. Eventually the parameter  $\alpha_{set}$  describes the amount of settling with a range of 0.1 to  $10^{-5}$ . The dust settling changes the corresponding dust scale height with respect to the gas scale height. Eventually the settling results in a local variation of the dust-to-gas-mass ratio. A low value for  $\alpha_{set}$  means that the dust is less homogeneously mixed with the gas and thus strongly settled.

Figure 3.2 shows that the higher  $\alpha_{set}$  (meaning that more equally distributed dust grains are present), the less water there is in the outer part of the disk. Again this can be explained by photo-desorption. When  $\alpha_{set}$  is lower, dust grains in the disk are said to be more inhomogeneously concentrated in the midplane, the medium is less optically thick. This means that the probability that radiation travels through the disk is higher. This radiation can cause water in ice form present on the grains to transfer back into the gas by photo-desorption.

### 3.3 Structure of the disk

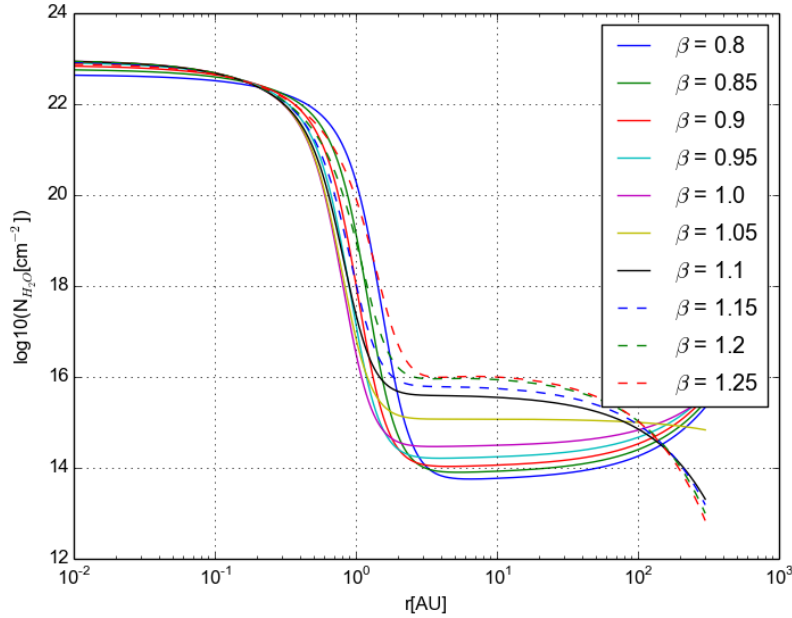


Figure 3.3: The change in parameter  $\beta$  and the resulting water profiles.

The flaring is described by the parameter  $\beta$ , which is related to the geometrical shape of the disk. It describes the power law with which the scale height of the disk changes as a function of radius  $r$ . To understand the effect of flaring, low values of  $\beta$  ( $< 1$ , flat disks) and high values of  $\beta$  ( $> 1$ , flared disks) were used in this study.

Figure 3.3 shows that more flaring, results in more gas phase water in the disk, but eventually less in the very outer parts of the disk. This last effect will be explained in section 3.5. In case of a flatter disk, less radiation intercepts with the disk and penetrates to the grains so causes less photo-desorption and returns less water to its gas phase again.

### 3.4 Dust grain sizes and size distributions

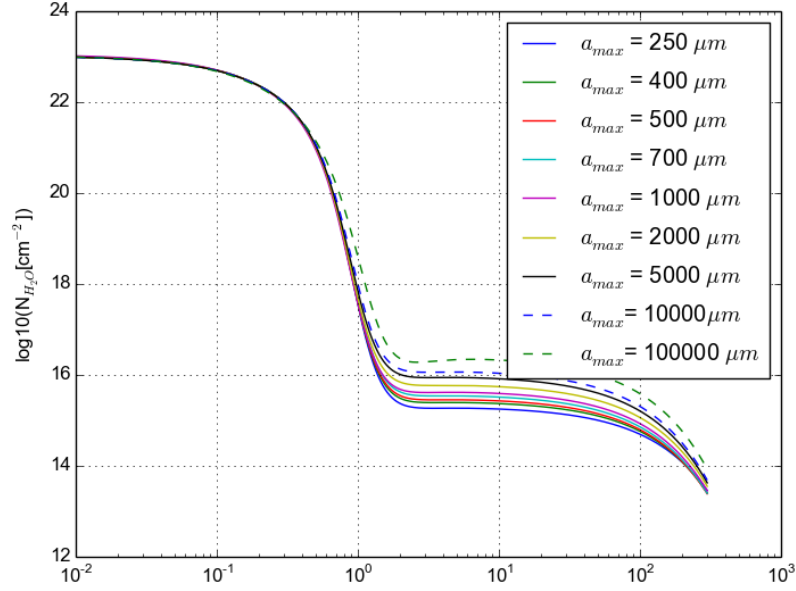


Figure 3.4: The change in parameter  $a_{max}$  and the resulting water profiles.

The maximum grain size and the dust size power law index are closely related. A range from 250 to  $10^5 \mu m$  has been looked at for  $a_{max}$ . The power law index,  $a_{pow}$ , has been looked at for values ranging from 2.0 till 4.5. This means that the smaller the power law index, the higher the fraction of the total dust mass in big grains, thus a decreasing UV opacity of the dust.

Figure 3.4 shows that when the maximum grain size is larger, there is more water in gas phase present in the outer parts of the disk. A larger maximum grain size results in more opacity and hence more photo-desorption. This is related to  $\alpha_{pow}$ . Figure 3.5 shows that if the mass of the dust grains increases in the amount of small grains the water profile has less water in the outer parts of the disk. This makes sense, because this means that there are more small grains present. Many small grains combined have more surface than the same amount of mass in bigger grains, which means that the opacity is higher and that less radiation can penetrate in to the disk resulting in less photo-desorption of water in the outer parts of the disk.

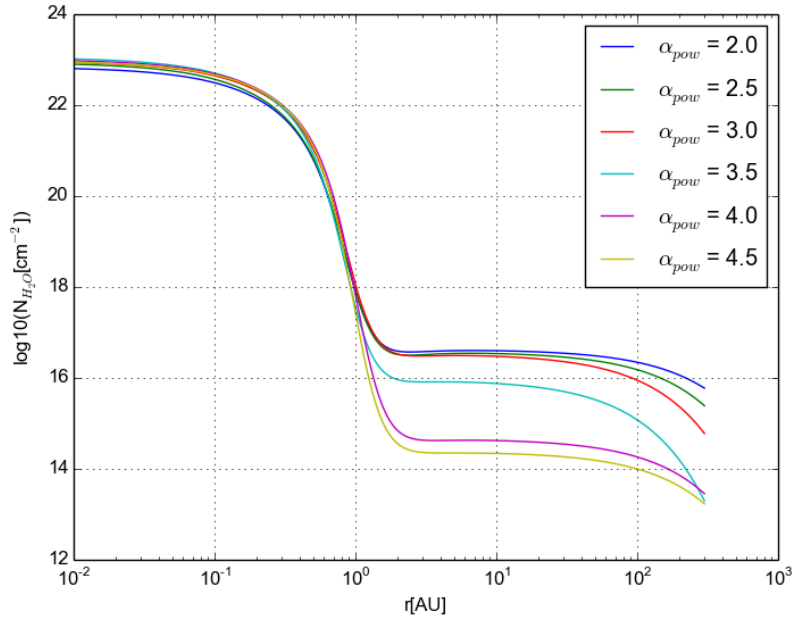


Figure 3.5: The change in parameter  $\alpha_{pow}$  and the resulting water profiles.

### 3.5 The Interstellar medium UV radiation field

The strength of the UV radiation field in the model is given in units of  $G_0$ . The models are spanning from less than our solar neighborhood ( $0.5G_0$ ) up to  $10^6G_0$ , which occurs in extreme cases like the Orion Bar or in active galaxies. These could also host protoplanetary disks as part of the star formation process.

Figure 3.6 shows that increasing the UV radiation field by a million times has little effect on the water column density in the outer part of the disk, the amount of water vapor is only slightly increasing. However, there is a strong increasing cut-off in the most outer disk. The inner disk (optically thick) is protected from radiation by the surface of the disk (which consists of optically thin dust, a molecular layer and an atomic layer). However, in the outer part of the disk, the radiation react with the disk. As the disk is more optically thin here, the water in the disk is photodissociated into other species (like H and OH) due to interstellar medium UV photons.

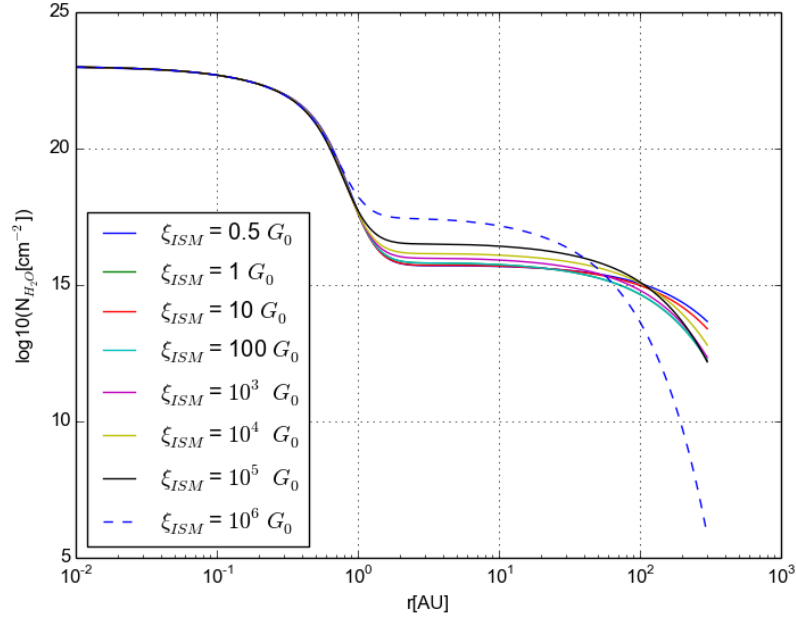


Figure 3.6: The change in parameter  $\chi_{ISM}$  and the resulting water profiles.

Looking back to the earlier discussed parameters, the process of photodissociation has visible effect in the most outer parts of all disks. The processes of photodesorption and photodissociation occur in parallel. If the number of photons increases or the medium becomes more optically thin, photodesorption increases but also photodissociation of water. So eventually, a higher photon flux causes a lower water gas phase column density. This effect is clearly seen in the flaring parameter ( $\beta$ ) and the dust-to-gas mass ratio ( $d/g$ ). Note that the settling parameter ( $\alpha_{set}$ ) does not show this behavior, there is no clear reason for this.

### 3.6 PAHs in disks

The parameter describing the PAH's molecules in the disk is  $f_{PAH}$ .  $f_{PAH}$  represents the fraction of the PAH's relative to the ISM abundance ( $\sim 3 \times 10^{-7}$  per H nucleus). This parameter spans from  $10^{-4}$  to 1.0. The PAH abundance can affect the fluxes of emission lines for the upper layers of the disk or in optically thin regions. In the current implementation, the

PAH parameter only affects the heating of the gas and is not treated as an additional opacity source. From plotting the results (see figure 3.7) it can be directly inferred that the PAHs do not change the water gas phase profile of the disk.

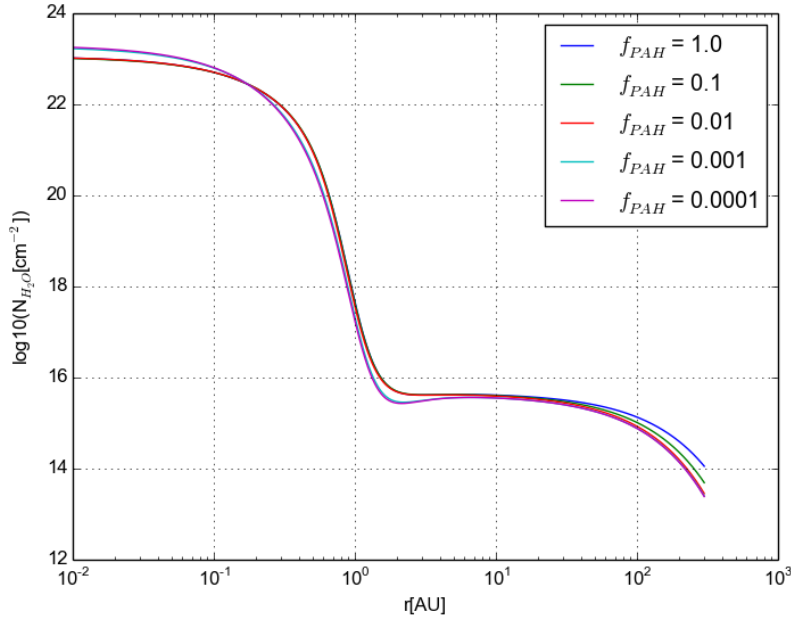


Figure 3.7: The change in parameter  $f_{PAHs}$  and the resulting water profiles.

### 3.7 Gas masses

The gas mass parameter ranges from  $10^{-5}$  to  $0.1 M_{\odot}$ . The dust-to-gas mass is kept constant and thus the dust mass scales with  $d/g = 0.01$ . Presently this regime brackets the observed mass range of protoplanetary disks. The gas mass parameter is determined by specific line observations or by the submm continuum of the dust, using dust-to-gas mass assumptions. In figure 3.8, it can be seen that if the gas mass increases, so does the column density of water. When the gas mass increases, the inner limit of the snow-line shifts to larger radii. Earlier in this thesis it is seen that the water mass in the disk comes mainly from inner part of the disk. Hence, with increasing gas mass more water mass will be found in the inner part of the

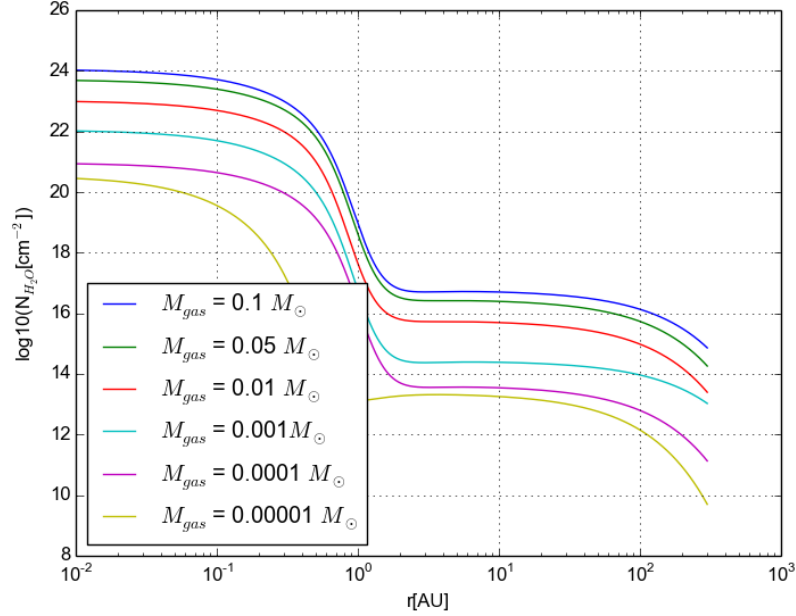


Figure 3.8: The change in parameter  $M_{gas}$  and the resulting water profiles.

disk. It makes sense for the snow-line to shift to larger radii as the gas mass increases, because now the temperature is systematically increasing at all radii due to the increasing gas pressure. Also visible in figure 3.8 is that the relative decrease of the amount of gas before and after the snow-line is approximately the same. This is because no other parameters have been changed; less gas in the inner part of the disk results in less gas in the outer parts. There is one more important observation to address for figure 3.8. Less gas mass gives less opacity because the  $d/g$  ratio is kept constant, so less gas mass means less dust mass and hence a lower continuum opacity and radiation can penetrate deeper resulting in less water in gas phase in the outer parts of the disk.

### 3.8 $\alpha$ and the Snow region

When running the script to calculate the fits (section 2.3.2) for all the above described parameters the  $\alpha$  parameter was needed, the parameter that describes the outer part of the snow region (equation 2.5). The parameter was

handpicked to always have a value between 1.5 and 3. Most of the time the shape of the fits did not change a lot whether the value 2 or 3 for  $\alpha$  was chosen to derive the best fit (section 2.3.3). When choosing a value outside the limit of 1.5 to 3, this resulted in larger deviations from the water column density data in most of the cases, and therefore it was better not to select such a value.

Therefore, the conclusion on the  $\alpha$  value (inducing a transition region) is that it is predominantly present to get a better fit to the data.  $\alpha$  is a numerical parameter without physical meaning that only ensures the presence of a transition region.  $\alpha$  can be changed over a range of values to recover within our function fitting process (which is already the best opportunity) the best fit again, but this is not the scope of the thesis.

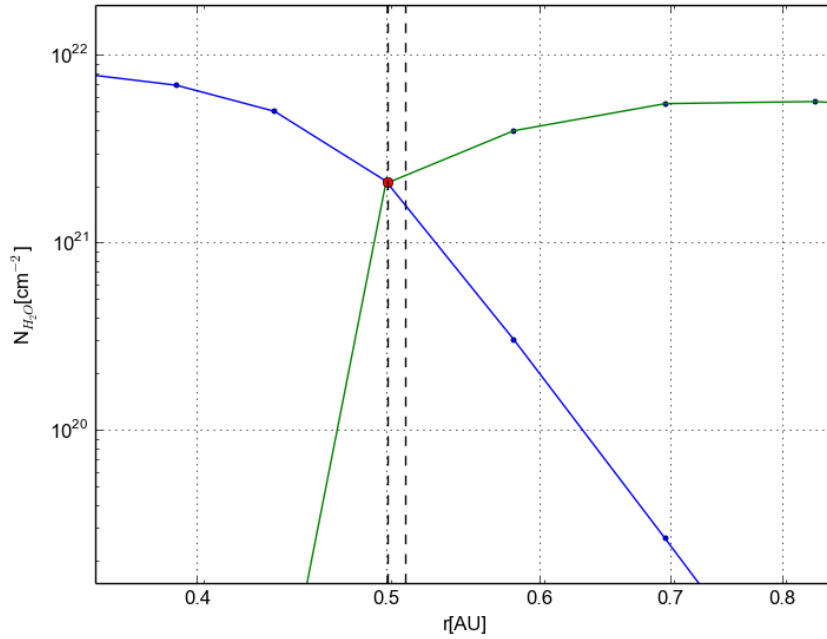
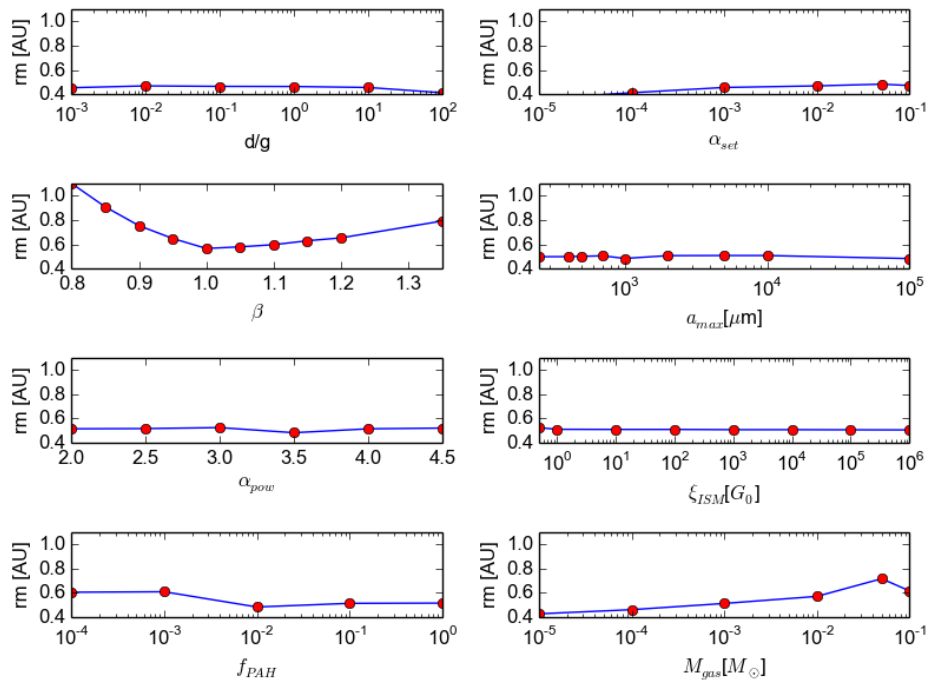


Figure 3.9: The  $rm$ 's are the black dotted lines, green: water in ice phase, blue: water in gas phase.  $rm$  is radially unresolved.

To recap it may be useful to summarize the ideas on the snow region so far: it starts at the intersection of the water gas column density and ice column density ( $rm$ ) and ends at  $\alpha \times rm$ . The snow region ends where  $\alpha = 1.5 - 3$  and it is just only there to fit better. The relevant quantity that comes out of the data numerically is  $rm$ . Table 2 of the appendix lists all the values of  $rm$  for the parameter changes of the previous sections. So, do any of the parameters influence  $rm$ ?

As one can see from table 2 in the appendix, the changes in  $rm$  caused by adapting the parameters are small. To consider whether it is useful to investigate these changes further the radial resolution of the computational grid is considered. For example, when taking  $a_{max} = 250\mu\text{m}$  and  $a_{max} = 10000\mu\text{m}$  the  $rm$ 's are respectively 0.498 and 0.508 AU. If there are multiple data points between the two radial values, it should be considered useful to look at the relations between parameters and  $rm$ . Otherwise  $rm$  is likely just a result of the limited radial resolution in the program as in the example of  $a_{max}$ , figure 3.9.

In figure 3.10 the relations between the physical parameters and  $rm$  are shown plotting everything on the same y-scale. For most cases the grid resolution is too poor and the relations have no meaning. However this figure points out that  $\beta$  and  $M_{gas}$  can be related to  $rm$  (outer radius), these two parameters change significantly enough that they must represent true relations. For  $\beta$  values smaller than 1,  $rm$  decreases with increasing  $\beta$  and for  $\beta$  values larger than 1,  $rm$  increases with increasing  $\beta$ . The decrease of  $rm$  is due to the decrease of the pressure (the disk becomes vertically thinner) when  $\beta$  increases up to  $\beta = 1$ . The increase of  $rm$  is due to the increase of photodesorption when  $\beta$  increases (if  $\beta > 1$ ). By increasing the total gas mass ( $M_{gas}$ ),  $rm$  increases due to an increase of pressure as explained in section 3.7. These two relations do hold, which will be useful when discussing this in the context of water line fluxes further on.

Figure 3.10:  $rm$  as a function of physical parameters.

## Chapter 4

# Water Emission Lines

The water emission lines are a direct output from the ProDiMo code and vary for different water distributions in the disk. This is of great interest, as astronomers often look at Spectral (Line) Energy Distributions (SLEDs) most of the time, which contain information on the properties and the origin of an object. In this chapter, the parameter influences on the water emission lines and a way to study the water emission lines from disks in the context of the snow line will be investigated.

### 4.1 Ortho- and Para-water

Water can actually be distinguished in two different species. As every hydrogen atom in water has a magnetic moment associated with the protons spin of  $1/2$ , the two hydrogen-protons in water ( $H_2O$ ) may possess a parallel(ortho) or anti-parallel(para) nuclear spin. Ortho-water has a magnetic moment of 1 (this is the high spin triplet state with three symmetric spin states  $+1, 0, -1$ , where the three states have equal energy in a zero magnetic field) while para-water has a magnetic moment of 0. Therefore para- $H_2O$  does not interact with an external magnetic field, but ortho- $H_2O$  does.

Conversion between these isomers is symmetrically forbidden for isolated water molecules. They can, however, change spin state by interacting with another particle, including other water molecules. At 0 K all spin states are in the para-state (lowest energy, no rotations) and the ratio shifts to the most stable statistical equilibrium ratio of 3:1 ortho-to-para at higher temperatures. It takes several months to reach this equilibrium in ice or gas or nearly an hour in ambient water. It is presently thought that the

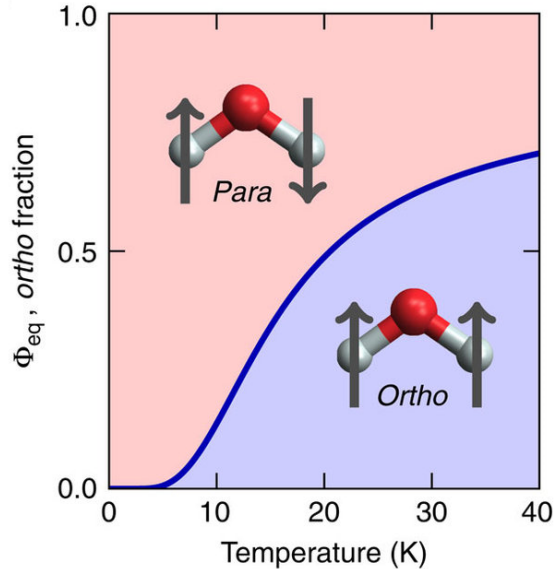


Figure 4.1: Ratio of para- and ortho-water as a function of temperature [11].

ortho-to-para ratio lies far from equilibrium and much closer to 1:1 in liquid water due to hydrogen bond formation [11]. In the protoplanetary disk  $H_2O$  exists in gas and ice phase and effectively consists of a mixture of non-identical molecules which must be taken into account when looking at the water emission lines.

## 4.2 Water lines

The emission lines of a disk model can be easily extracted from the output data of the code for every species, and ortho- and para-water are no exception. Both will be considered in the further research of the vapor gas emission spectrum. Water has a lot of quantum states which results in thousands of possible energy transitions, i.e. emission lines that occur when the molecule goes to a lower energy state and emits a photon. All those lines together form the SLED which is shown in figure 4.2, the water emission vapor flux versus wavelength. Note that the continuum of the SLED is not displayed, i.e. the lines normally lie on top of the continuum.

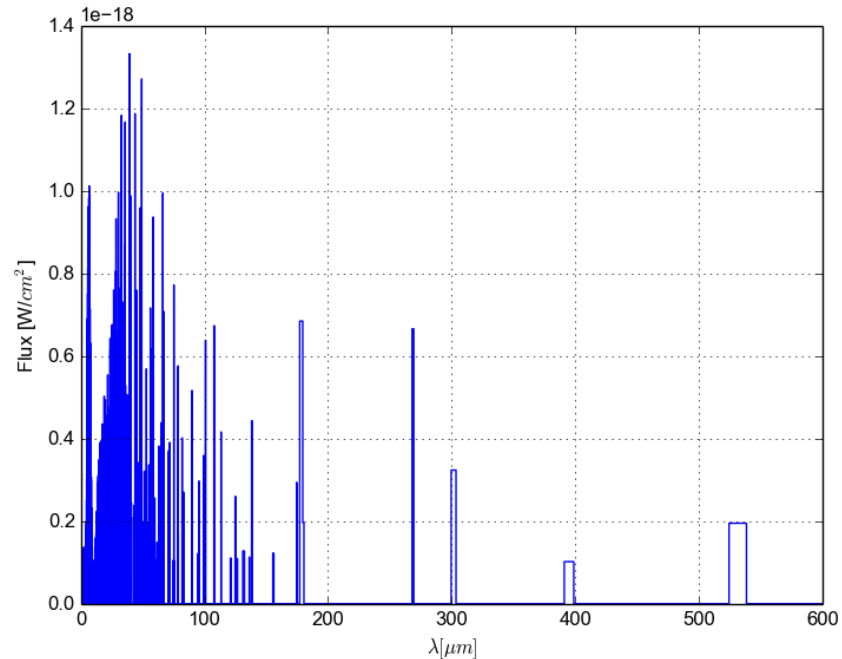


Figure 4.2: Water vapor emission flux versus wavelength of the  $a_{max} = 250\mu\text{m}$  model.

Figure 4.2 shows that there are a lot of lines at short wavelengths ( $\lambda$ ). To inspect the vapor water flux versus the wavelength more precisely, it is better to plot it on semi logarithmic scale shown in figure 4.3

In figure 4.3 roughly three regimes of transitions appear in which all the lines are created due to a combination of rotational and vibrational transition of levels. Note that, by keeping in mind the well-known formula  $E = h \cdot \nu = h \cdot c/\lambda$  (where  $c$  is the speed of light,  $\nu$  the frequency or  $\lambda$  the wavelength of a photon) long wavelengths have less energetic photons. The water level population of all the different quantum states determines the strength of the different water lines at a certain radius. To get a water molecule in a certain level a certain excitation temperature is needed and the higher the temperature, the higher the level. Energy is emitted in the form of a photon when a spontaneous transition to a lower level occurs, this is denoted as emission radiation. The energy difference between two levels determines the energy and therefore the wavelength of the photon. It is

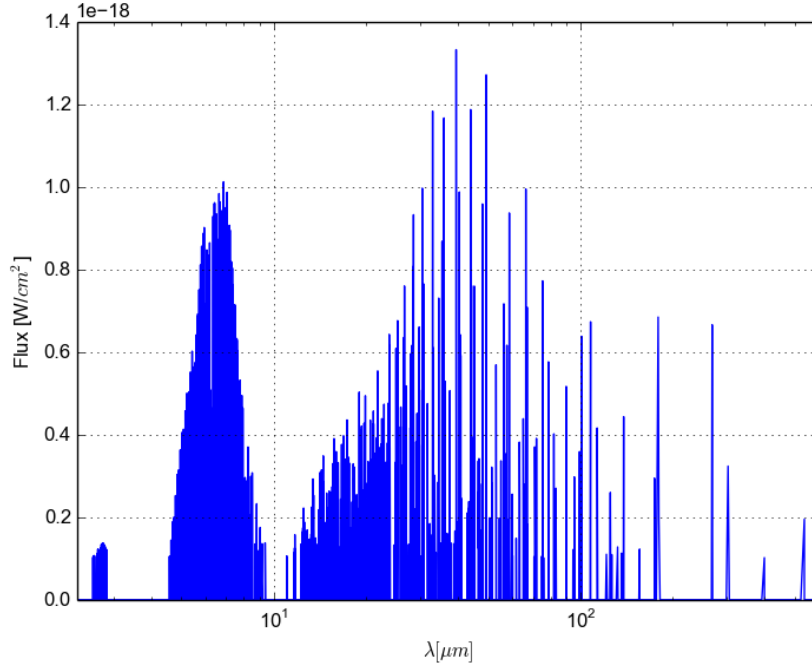


Figure 4.3: Water vapor emission flux versus wavelength of the  $a_{max} = 250\mu\text{m}$  model in semi log-space.

in the intrinsic nature of water, that at low temperatures water produces longer far-infrared/submm wavelengths and at high temperatures shorter mid-infrared wavelengths. Since in protoplanetary disks the gas temperature in the outer disk is lower, long wavelengths come from larger radii from host star and short wavelengths come from the smaller radii from the host star. This is discussed in more detail in the paper of Antonellini et al. (2015).

In the paper of Zhang et al.(2013) specific prominent lines were selected, because not all lines can be seen with present-day technology. Protoplanetary disks are relatively small astronomical objects and therefore a high sensitivity is needed to pick up good data for making images. However, observations of water lines are of importance in this thesis and need to be done in space due to the earths atmosphere, it absorbs water lines because it contains water. Also the spectral resolution needs to be high because the narrow emission lines need to be resolved. The James Webb Space Telescope (JWST) will have a spectral sensitivity up to  $10^{-24}$  W/cm<sup>2</sup> which is

good. But not only a high spectral resolution will do the job, light can be blocked or attenuated/scattered by other objects. Note also that the flux from the water emission lines is only a small fraction to the total flux of the protoplanetary disk. Because of these limitations it is currently very difficult to find the water emission lines. Our best hope is to look at some specific strong water lines, which are visible with the current observational methods. Therefore it is convenient to restrict this study to a few strong water emission lines.

In figure 4.4, the six chosen specific regimes with strong water emission lines are shown. In addition, the total flux received from the regimes is visible in the upper right corners of the plots (this is the sum of all the line fluxes in that regime). Line fluxes which were lower than  $10^{-19}$  W/cm<sup>2</sup> have not been taken into account in this figure as they do not contribute much to the total flux. The specific lines analyzed in this thesis are shown in figure 4.4 and the corresponding quantum numbers of each transition are shown in the appendix table 3.

Now that some grip is obtained on the many water emission lines by looking at some specific regimes where strong emission fluxes come from, some specific prominent and promising emission lines can be picked out. The flux of these lines will change per model because the structure of the disk changes. Therefore we can use these lines as finger prints and investigate how they change with different parameters. Four lines from the six regimes to compare to each other are chosen: the 17.22, 30.8, 63.3 and the 179.5  $\mu$ m lines. The 17.22 and 30.8  $\mu$  lines are actually line blends. The 30.8 blend and the 179.5  $\mu$ m line are pure ortho-water lines. The 179.5  $\mu$ m line is the transition line from the second excited rotational level to the first excited level, while the other lines are all much higher excitation lines. No strong emission lines come from vibrational transitions. The 17.22  $\mu$ m blend has typically an energy of 2,500 - 5,800 K and the 30.8 $\mu$ m blend of 900 - 1,000 K. The 63.3  $\mu$ m line has an energy around 1,000 K and the 179,5  $\mu$ m line of 100 K. The 17.22 and 30.8  $\mu$ m blend can therefore be denoted as inner disk lines and the 63.3 and 179.5  $\mu$ m lines as outer disk lines, because, as discussed before, these longer wavelengths come from the outer part and the short wavelengths come from the inner part of the protoplanetary disk. Hence the lines can react differently to parameter changes as will be seen in the next section.

With the data, the two line fluxes and two blends were calculated for

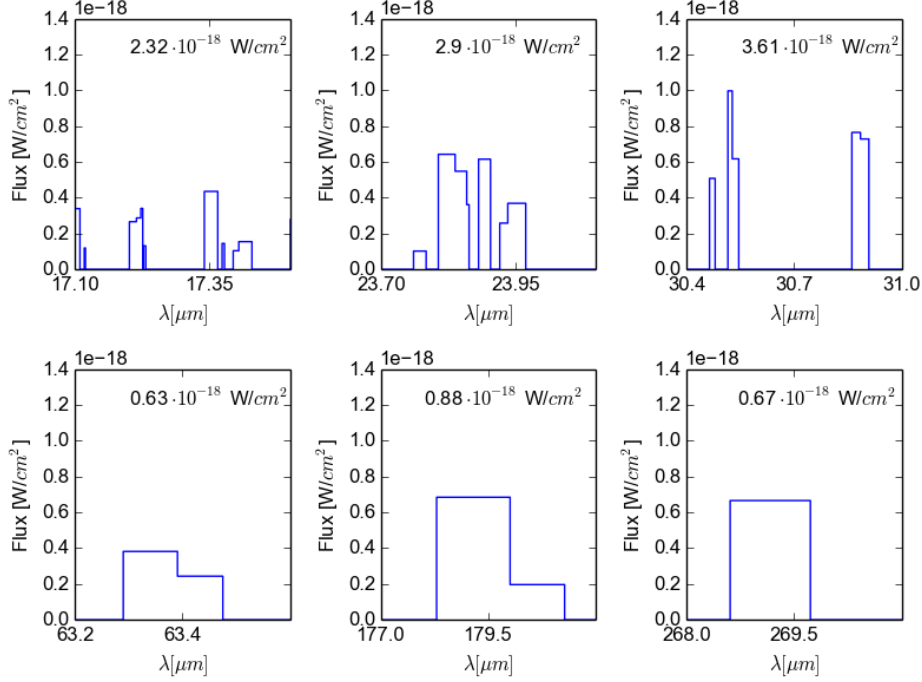


Figure 4.4: Water vapor emission flux versus specific wavelength regimes of the  $a_{max} = 250 \mu\text{m}$  model.

all models as well as the ratios between those fluxes. In the latter case, line fluxes were taken into account even when they were smaller than  $10^{-19} \text{ W/cm}^2$ . This will be used in the following section to infer the relations between the parameters and the water gas fluxes (ratios).

### 4.3 Changing parameters and emission

All the calculated line ratios are shown in table 4 of the appendix. In addition, the corresponding  $17.22 \mu\text{m}$  line flux is shown for completeness, in order to distinguish if a change in ratio is because of the change in the  $17.22 \mu\text{m}$  line or because of change in one of the other lines. Since the gas mass and the flaring parameter can be related to the position of the snow line, a separate section will be used to discuss the position of the snow line and the emission lines.

Different graphs have been made for the different parameters in this section. The chosen line ratios are plotted in a 3D graph. The color of the spheres indicates the value of the varied parameter. Also the importance of the 17.22  $\mu\text{m}$  line flux is taken into account: The size of the spheres scales with the line flux. The size of the symbol is scaled by the line flux in units of  $10^{-20}$   $\text{W}/\text{cm}^2$ . In some cases where the line flux varies over more than one order of magnitude, the logarithm of the flux in units  $10^{-21}$   $\text{W}/\text{cm}^2$  is used. These figures are made to show overall relations, exact values can be found in the appendix table 4.

### 4.3.1 Small changing 17.22 line

The settling is represented in figure 4.5. All ratios decrease, however the outer lines decrease more than the inner lines when  $\alpha_{set}$  decreases. There are irregular behaviors in the decrease of the 63.3 and 179.5  $\mu\text{m}$  lines which are probably due to the way settling in the disk happens (the positions). Note that the 17.22  $\mu\text{m}$  line does not change much over the range of the parameter. Less water is seen due to a higher  $\alpha_{set}$ . More settling or a lower  $\alpha_{set}$ , which means less homogeneously mixed dust grains, causes an increase of all water lines concerned. As explained in section 3.2, the opacity drops due to strong settling. Removing the opacity may also increase  $T_{gas}$ , leading to brighter water lines.

Figure 4.6 shows the effect of the  $f_{PAH}$  parameter on the water lines. From chapter 3 it is known that the number of PAHs does not change the amount of water in the disk significantly. However, a decrease in the water line ratios is visible when the number of PAH's decreases. The 17.22  $\mu\text{m}$  line does not change much. The 30.88  $\mu\text{m}$  line decreases the most and is followed by the 63.3 and the 179.5  $\mu\text{m}$  line. So the PAHs have more influence on the 30.88  $\mu\text{m}$  line than on the others. More PAHs increase  $T_{gas}$  and this can result in larger emitting areas, which causes more water emission to be seen even if there is as much water in the disk as before.

The flaring parameter has a similar way of changing line ratios as the PAHs graph, an increase in flaring increases the line ratios, but in this case also the 17.22  $\mu\text{m}$  increases significantly. In figure 4.7 this effect is shown. Because of the flaring, more radiation from the host star can warm up the disk, which again results in more visible water. Note that there is actually less water in the very outer disk this time due to the process described in 3.5.

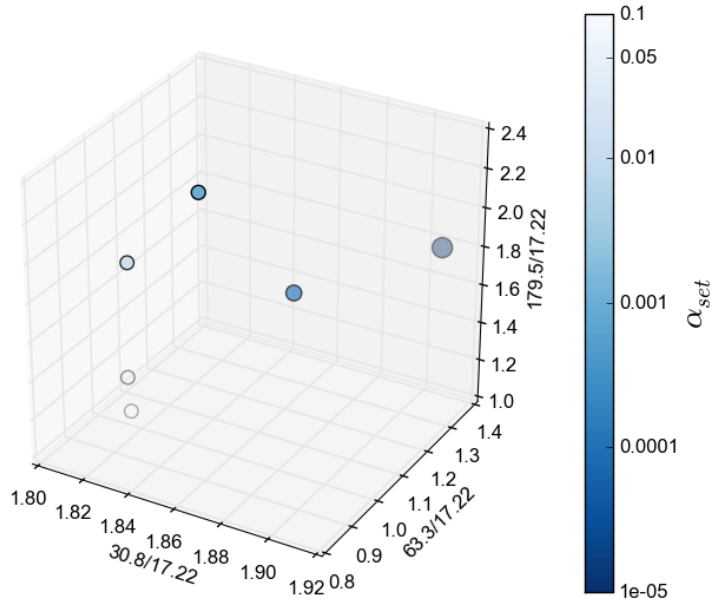


Figure 4.5: Line ratios and the settling parameter.

In figure 4.8, the relation between the flux ratios and the maximum grain size is shown. All ratios decrease with increasing maximum grain size. The 30.8/17.22 line ratio decreases but has a turnover due to its value at  $a_{max}=100000 \mu\text{m}$ . The 17.22  $\mu\text{m}$  line increases with increasing maximum grain size by a factor 10, but all the line ratios decrease a factor  $\sim 2$ , so actually all the other lines decrease when the maximum grain size increases (the inner lines more than the outer lines). A large maximum grain size results in observations of less flux of the 30.8, 63.3 and 179.5  $\mu\text{m}$  lines because then it makes the disk optically thinner as explained in section 3.4. The increase of the 17.22  $\mu\text{m}$  line is explained in the next section and is also due to a decreasing opacity.

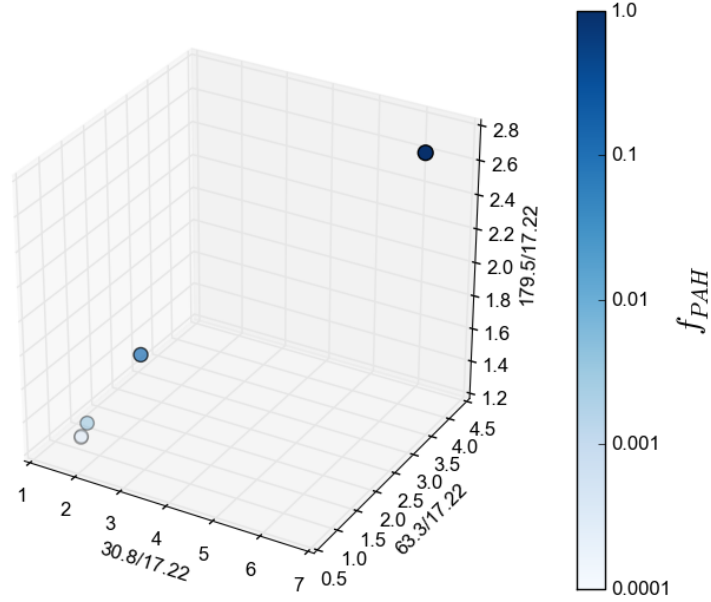


Figure 4.6: Line ratios and the number of PAH's parameter.

### 4.3.2 Large changing 17.22 line

In figure 4.9 the varying dust-to-gas mass parameter is shown. All the line ratios decrease when the dust-to-gas mass ratio is decreasing. The longer the wavelength of the line, the larger the decrease. Note that the 17.22  $\mu\text{m}$  line increases three orders of magnitude when decreasing the dust-to-gas mass ratio. Therefore it seems that all these ratios decrease because of the increase of the 17.22  $\mu\text{m}$  line. Nevertheless, in the line ratios from the models with  $d/g = 10$  and 100, the 30.8, 63.3 and 179.5  $\mu\text{m}$  lines seem to decrease by themselves. The gas mass stays constant in all models, and to change the dust-to-gas mass ratio, dust is removed or added to the model. Less dust makes the disk more optically thin. However, by better investigation, all the line ratios decrease due to increasing gas mass, which is caused by the 17.22  $\mu\text{m}$  line increase.

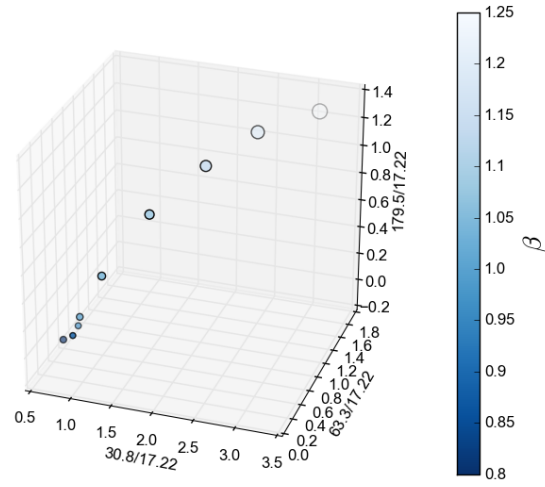


Figure 4.7: Line ratios and the flaring parameter.

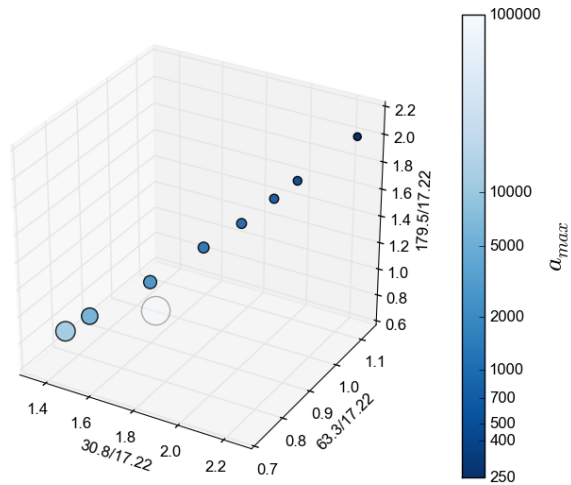


Figure 4.8: Line ratios and the maximum grain size parameter parameter.

An optically thick line will not change its flux when there is more column density in the disk. In principle all lines in the disk are optically thick, but the dust continuum intercepts with the lines from the inner disk because of the geometry of the disk: the layer of gas is smaller in the inner disk than the layer of gas in the outer disk on the dust continuum. So the inner water lines reach the continuum opacity before the line reaches the column density to become optically thick, this is schematically shown in figure 4.9. So when the dust decreases, the inner lines, such as the  $17.22 \mu\text{m}$  line, can use more water column density to become optically thick and hence emit much more flux. This is the effect that explains figure 4.10.

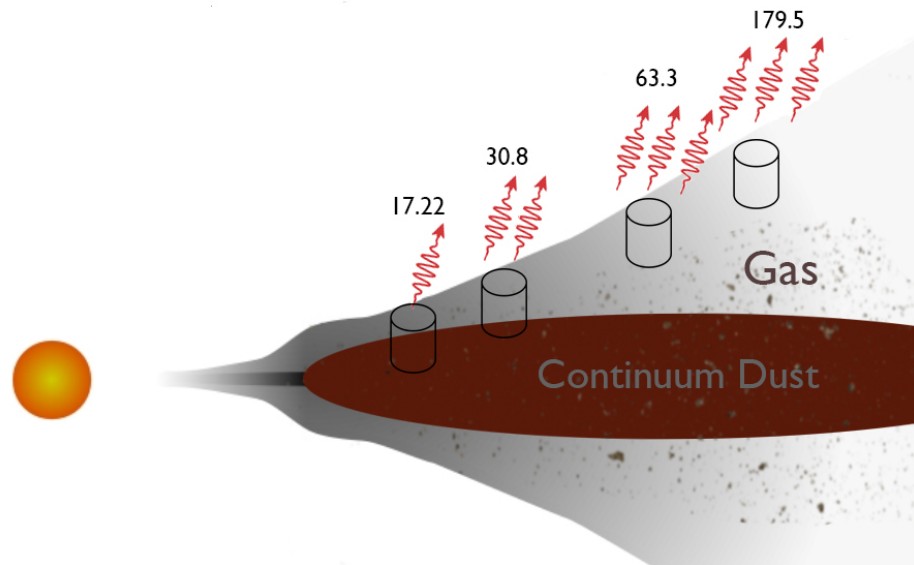


Figure 4.9: Schematic image of how dust influences the water vapor lines (in  $\mu\text{m}$ ) in the disk.

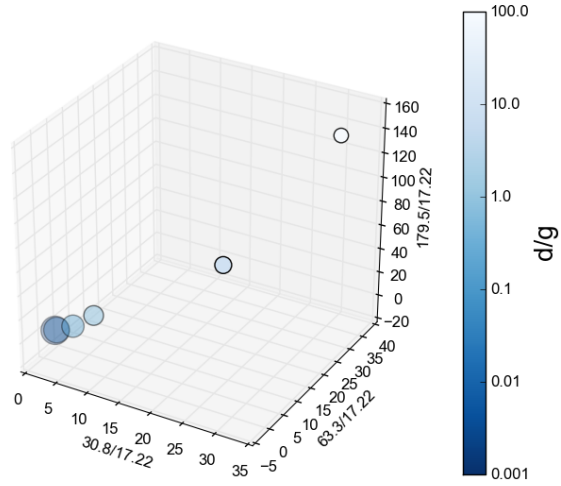


Figure 4.10: Line ratios and the dust-to-gas mass ratio parameter.

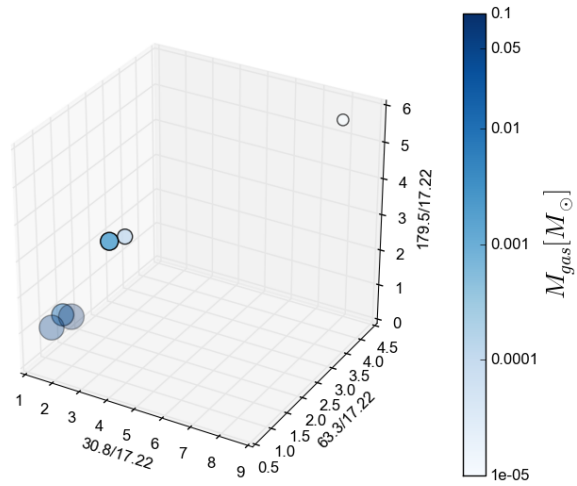


Figure 4.11: Line ratios and the gas mass parameter.

The gas mass parameter and its line ratio changes are shown in figure 4.11. All ratios decrease when the gas mass is increased. However, there are irregular behaviors in all ratios. The 17.22  $\mu\text{m}$  line is again increasing three orders of magnitude when increasing the gas mass. Therefore inferring that the ratios decrease predominantly because of the increase of the 17.22  $\mu\text{m}$  line. Here the same process occurs as in the dust-to-gas mass case described in the previous paragraph.

In figure 4.12 the relation with the power law index is shown. The 30.8/17.22 and the 63.3/17.22 line ratios decrease with increasing  $\alpha_{pow}$ , while the 179.5/17.22 increases. The 17.22  $\mu\text{m}$  line flux decreases two orders of magnitude with an increasing  $\alpha_{pow}$ . This means that the 30.8 and 63.3  $\mu\text{m}$  lines must decrease by themselves while the 179.5/17.22 line ratio increases due to the fact that the 17.22  $\mu\text{m}$  line decreases, the 179.5  $\mu\text{m}$  does not change significantly. The latter occurs too for the 292.2  $\mu\text{m}$  line, the transition of the first excited state of para- $H_2O$  to the ground state, which is shown in table 4 of the appendix. Note that the shorter wavelengths contain irregular behaviors in the graph. To conclude, if  $\alpha_{pow}$  decreases, there is a higher fraction of the dust in big grains present and hence short wavelengths become more prominent (disk becomes more optically thin and contributes to the short wavelengths as discussed in the paragraph about  $d/g$ ), while there is more water in the outer parts of the disk (section 3.4).

The last parameter that remains to be discussed is the UV radiation influence on the water vapor emission lines (see figure 4.13). The 30.8/17.22 line and 63.3/17.22 ratios increase when the amount of radiation applied to the disk, increases. The flux of the 179.53/17.22 line ratio decreases when  $\xi_{ISM}$  increases, however the ratio shows a large increase before this decrease. The other line ratios also show this irregular behavior. In addition, the 17.22  $\mu\text{m}$  line increases two orders of magnitude while increasing the UV radiation and therefore the 30.8 and 63.3  $\mu\text{m}$  lines as well. The 179.5  $\mu\text{m}$  wavelength probably decreases because of the increase of the 17.22  $\mu\text{m}$  line. UV radiation breaks down water in the outer disk, so less water is there at high  $\xi_{ISM}$  as discussed in section 3.5. However, as it is also warmer, lines from nearby the host star will gain a larger emitting area resulting in more radiation.

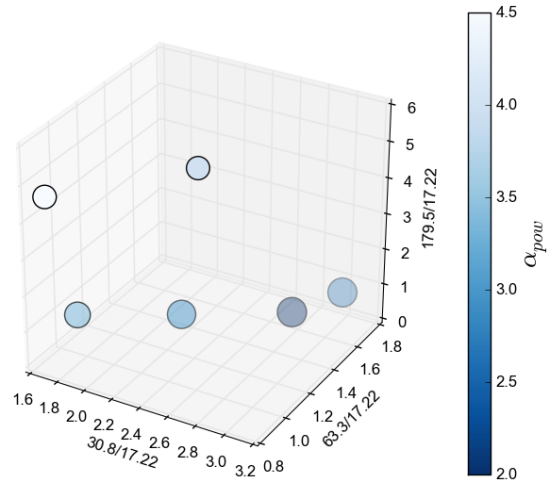


Figure 4.12: Line ratios and the dust size distribution power law parameter.

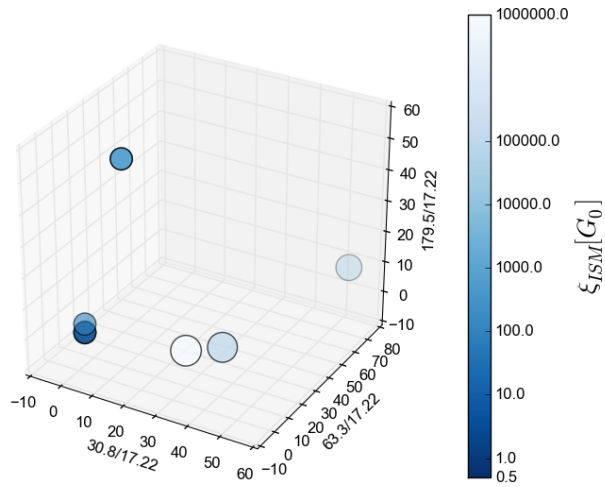


Figure 4.13: Line ratios and the UV radiation parameter.

#### 4.4 The Snow line and emission lines

As stated in section 3.8, the gas mass and the ( $\beta$ ) flaring parameter change the position of the inner limit of the snow region. This means that graphs can be made that show the relation between the snow line position and the emission line ratios (see figure 4.14 and 4.15). With these graphs it may be possible to use the lines or line ratios to deduce the inner position of the snow region.

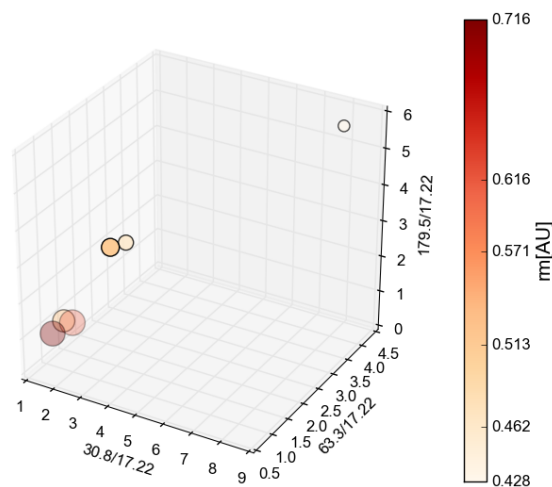


Figure 4.14: Line ratios and  $rm$  based on the  $M_{gas}$  model.

In figure 4.13 the irregular behaviors are still present due to the fact that this figure is based on the gas mass parameter. Figure 4.14, which is based on the flaring parameter, is more interesting because here a straight line can be seen which indicates a direct relation between  $rm$  and the observed line ratios. However,  $rm$  is first decreasing with increasing flaring and then increasing again. The switching point is where  $\beta$  becoming larger than 1.

It is not completely clear if the line ratios of the observations can really say something about the position of the snow line. To investigate this better all graphs were combined in figure 4.16. The size of the  $17.22 \mu\text{m}$  line flux is not taken into account in this graph anymore for simplification purposes, all the dots were given the same size. The most outer left point shows

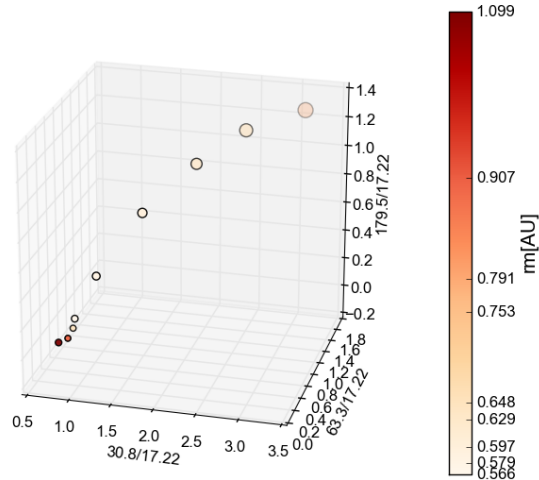


Figure 4.15: Line ratios and  $rm$  based on the  $\beta$  model.

the highest value for  $rm$  and proceeding to the right, the values for  $rm$  seem to be decreasing. This indicates there is a tentative relation with the position of the snow line ( $rm$ ): the higher the line ratios, the lower the  $rm$ . A singular value decomposition is done to make a straight line through the data, resulting in respectively 0.394805, 0.55581547, 0.7315724 as slopes for the logarithmic 30.8/17.22, 63.3/17.22 and 179.5/17.22 line ratios, i.e. the direction vector of the best fit line in least squares sense. Note that this vector has to be moved to the mean of the data points. Nevertheless, looking at the middle of the graph, a messy bunch of data is seen. Also when this was a clear relation, all the points together would show a smooth rainbow pattern. However, it does look like there is a tentative relation which can be split up in two regions. A region with low line ratios and relatively large  $rm$  which shows a smooth decrease when increasing the line ratios and a region with small  $rm$  at high line ratios which is more like a random distribution of data points showing less relation with the line ratios in parameter space. Note that this graph shows that it would be interesting to investigate the first region more with observational data. Taking this into consideration, according to the ProDiMo code, the position of the snow region shows a tentative relation with the line ratios.

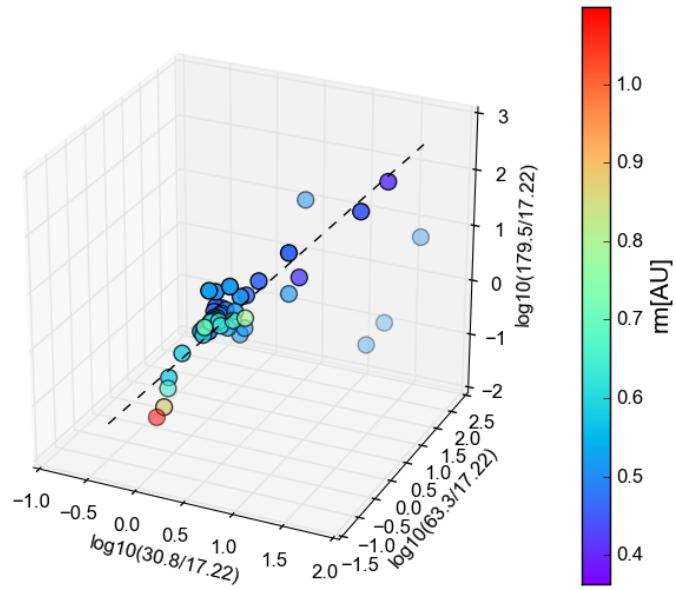


Figure 4.16: Line ratios and  $rm$  using all discussed parameters combined.

# Chapter 5

## Conclusion and Discussion

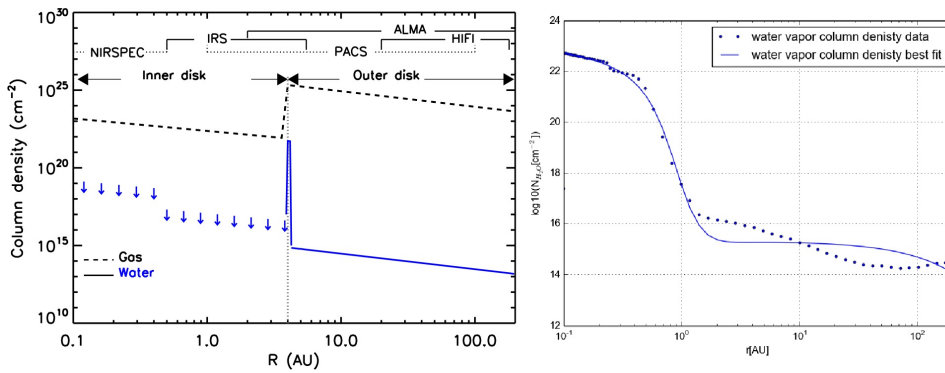


Figure 5.1: Left: The best-fit radial abundance of water vapor in TW Hya according to Zhang et al. (3013), illustrated by the vertically integrated column density profile (solid curve). Within 4 AU, the maximum water abundance is depicted by arrows. The dashed curve is the total gas column density. At the top of the figure, the role of the multi-wavelength observations in tracing different radii of the disk is shown. Right: The water vapor column density of the  $a_{max} = 250\mu\text{m}$  model and the best fit to this data by use of a snow region.

In this study the water column densities of a protoplanetary disk were calculated by using the ProDiMo code. In order to interpret the calculated column density profiles, multiple fits were made to match the water column density data. A method to fit the data as closely as possible was developed. The method was tested by calculating the cumulative mass function of the various fits. The conclusion of this test was that a simple step function for

fitting the water column density (as used by K.Zhang et al. (2013), figure 5.1) is an oversimplification for the data. A step function may by chance give a pretty good indication of the total mass of water in a protoplanetary disk, but this is not always the case. The shape of the fit is deviating very much from the observed water column density data. Therefore, a simple step function is not a good way to describe the water distribution in a protoplanetary disk. A multiple step function would be more accurate. But treating the snow line as a region in the fitting process does fit way better than the step functions.

The snow line is discussed and better defined by the concept of a snow region. The snow line was argued to look more like a transition region rather than it being a line and should therefore be described by two values. The  $rm$  parameter, which is calculated from the data as the intersection point between the water and ice column density, and the  $\alpha$  parameter, which describes the radial extent of the region so that it describes the point after which the water column density does not change significantly enough anymore (manually chosen), represents the inner and outer limit of the snow region respectively. As the step function does not take into account this second point it does not describe the water profile properly. The fit of the water profile model that is proposed which includes both points to describe the snow region (equation 2.5) resulted in the best fit to the observed data.

The ProDiMO model was subsequently used to vary different parameters associated with the appearance of the protoplanetary disk, in order to post-process the correlations between the parameters and the water column density. Equation 2.5 was fitted to all water in gas phase column densities. In table 5.1 the changes of the vapor water column density are summarized. The main processes behind the changing water profiles were opacity differences due to changes in the amount or size in dust which increased or decreased the amount of photo-desorption possible and the process of photo-dissociation due to high energy radiation.

The position of  $rm$  was also calculated as this is an intrinsic property of every model. The parameter  $\alpha$  was not, it was concluded that its main function is to better the fitting of a model and only ensures the presence of a transition region. The gas mass parameter ( $M_{gas}$ ) and the flaring parameter ( $\beta$ ) appeared to be correlated to  $rm$  and therefore also to the position of the inner limit of the snow region. For  $\beta$  values smaller than 1,  $rm$  decreases with increasing  $\beta$  and for  $\beta$  values larger than 1,  $rm$  increases with increasing  $\beta$ .

Parameter increase	inner disk ( $r < rm$ )	outer disk ( $r > \alpha$ )	very outer disk ( $r \gg \alpha$ )
$d/g$	-	↓	↓
$\alpha_{set}$	-	↓	↓
$\beta$	-	↑	↓
$a_{max}$	-	↑	↑
$\alpha_{pow}$	-	↓	↓
$\xi_{ISM}$	-	↑	↓
$f_{PAH}$	-	-	-
$M_{gas}$	↑	↑	↑

Table 5.1: Influence of the parameters on the water in gas phase column density. ‘-’ indicates no changes.

The decrease of  $rm$  is due to the decrease of the pressure when  $\beta$  increases up to  $\beta = 1$ . The increase of  $rm$  is due to the increase of photodesorption when  $\beta$  increases (if  $\beta > 1$ ). By increasing the total gas mass ( $M_{gas}$ ),  $rm$  increases due to an increase of gas pressure.

Zhang et al.(2013) presented an observational reconstruction of the radial water vapor content at the surface of the TW Hya protoplanetary disk and reported the first localization of the snow line. They fitted a two-dimensional disk model to the available star and disk photometry of all observed  $H_2O$  lines, using a simple step function parameterization of the water vapor content near the disk surface, which has already proven to be an oversimplification since the snow line is better described by a snow region. However it could still be tested whether the ProDiMO code, which contain a detailed chemistry, allows that the position of the snow region can be related to observational data, emission lines.

The water emission lines have been extracted from each model. By picking prominent water emission lines, coming from different parts of the disk (short  $\lambda$  small radii and visa versa), correlations between these emission line ratios and the parameters can be determined. In table 5.2 a summary is presented of these correlations. The physical processes behind explaining these relations can be found in the way dust influences the emission lines in the disk (more short than on long wavelengths) and the heating of the gas which results in more emission.

Parameter increase	30.8/17.22	63.3/17.22	179.5/17.22	17.22 $\mu$ m	30.8 $\mu$ m	63.2 $\mu$ m	179.5 $\mu$ m)
$\alpha_{set}$	↓	↓↓	↓↓↓	↓ small	↓	↓	↓
$f_{PAH}$	↑↑↑	↑↑	↑	↑ <i>small</i>	↑	↑	↑
$\beta$	↑↑↑	↑↑	↑	↑	↑	↑	↑
$a_{max}$	↓↓	↓	↓↓	↑	↓	↓	↓
$d/g$	↑	↑↑	↑↑↑	↓ large	-	-	-
$M_{gas}$	↓↓↓	↓	↓↓	↑ large	-	-	-
$\alpha_{pow}$	↓↓	↓	↑	↓ large	↓	↓	-
$\xi_{ISM}$	↑↑	↑	↓	↑ large	↑	↑	-

Table 5.2: Influence of the parameters on the water in gas phase emission lines. The amount of arrows indicates the relative in-or decrease of the line ratios. - indicates a line is not significantly changing

An indirect result of the study of the water emission lines and the disk parameters to address is that a high presence of short water emission wavelengths indicates bigger dust grains within the disk (hence less water in gas phase) and vice versa. This relationship deserves further investigation.

Since the snow region and the gas mass and flaring parameter are shown to significantly change  $rm$  (inner radius),  $rm$  and the water emission lines could be compared for these parameters. By doing so it was not completely clear that the line ratios can really say something about the position of the snow line. To investigate this better all parameter graphs with respect to the water emission line ratios were used to make a graph that shows the position of the snow region as a function of logarithmic line ratios (figure 4.16). From this graph was concluded there is a tentative relation between the snow region and the emission line ratios. So Zhang et al. (2013) were in a certain sense right to relate the emission lines to the position of the snow line.

The conclusions above have been based on the ProDiMo code, which has been a successful method in describing protoplanetary disks and their properties by what is known about these astronomical objects so far. It is very clear protoplanetary disk are complex objects in which many processes play a role, each with different relations to the water column density and the snow region. A mixture of different parameters compared to another totally different mixture of parameters could result in a similar water profile plus snow region. Also, their water emission ratios can be totally different or very similar, because many processes influence the properties of disk. Nevertheless a tentative relation of the snow line and the water emission line ratios has been found. As discussed changes of isolated processes could

be mapped, which was an advantage of the code used in this study. It would be interesting to investigate how changing the parameters of other disk-types would influence their water profile. Of course the physics will be the same, yet maybe some other parameters could be directly related to the position of the snow region. Another interesting idea for further research would be to look for a numerical way to describe  $\alpha$  through the output of the code, as this can give the snow line an even more reliable strict definition. Maybe the JWST will in the future be able to tell us more about the water in the protoplanetary disks, by for example confirm observationally that the tentative relation found in this thesis does hold.

## Chapter 6

# Appendix

Output calculations example data of  $a_{max} = 250\mu m$  model:

```
Intersection between water and ice column density
interpolated (r): [ 0.498]
Intersection between water and ice column density
in data (r), index: 0.49666399 30
Enter parameter alpha: 3
Approximately the start of the lower part by a
parameter alpha (r), index, alpha: 1.415444 36 3
Parameters for linear fitted functions:
a,b: [-3.30047131 23.02992879]
c,d: [-6.18700533e-03 1.53144906e+01]
Smoothness parameter to interconnect linear functions:
e: [ 1.00651277] Values for the 2 regimes of the step function:
a,b: [ 0.85227253 0.64199999]
Values for the 3 regimes of the 2 step function:
a,b,c: [ 0.85227253 0.62629084 0.71753735]
Percentage deviation of accumulated mass from fit,
step and the 2 step fuction: [-34.88356696 99.79999317 89.58100231]
```

Reaction	Type
$H_2 + OH \rightarrow H_2O + H$	Neutral-neutral
$NH + OH \rightarrow H_2O + N$	Neutral-neutral
$NH_2 + OH \rightarrow H_2O + NH$	Neutral-neutral
$NH_2 + NO \rightarrow N_2 + H_2O$	Neutral-neutral
$OH + OH \rightarrow H_2O + O$	Neutral-neutral
$OH + H_2CO \rightarrow HCO + H_2O$	Neutral-neutral
$NH_2 + H_3O^+ \rightarrow H_2O + NH_3^+$	Ion-neutral
$H_3O^+ + Si \rightarrow SiH^+ + H_2O$	Ion-neutral
$H_3O^+ + SiO \rightarrow SiOH^+ + H_2O$	Ion-neutral
$H_3O^+ + e^- \rightarrow H_2O + H$	Dissociative recombination
$H_- + OH \rightarrow H_2O + e^-$	Associative detachment
$H + OH \rightarrow H_2O + h\nu$	Radiative association
$H_3O^+ + h\nu \rightarrow H_2O + H^+$	Photodissociation
$H_2^* + OH \rightarrow H_2O + H$	Neutral-neutral
$H_2O_{ice} + dust \rightarrow H_2O + dust$	Desorption
$H_2O_{ice} + C.R.P. \rightarrow H_2O + dust$	Cosmic-rays-desorption
$H_2O_{ice} + h\nu \rightarrow H_2O$	Photodesorption
$PAH^- + H_3O^+ \rightarrow PAH + H_2O + H$	PAH dissociative recombination
$H_2O + H \rightarrow OH + H_2$	Neutral-neutral
$H_3^+ + H_2O \rightarrow H_3O^+ + H_2$	Ion-neutral
$C^+ + H_2O \rightarrow HCO^+ + H$	Ion-neutral
$CH_5^+ + H_2O \rightarrow H_3O^+ + CH_4$	Ion-neutral
$H_2O + Si^+ \rightarrow SiOH^+ + H$	Ion-neutral
$H_2O + HCO^+ \rightarrow CO + H_3O^+$	Ion-neutral
$H_2O + HN_2^+ \rightarrow N_2 + H_3O^+$	Ion-neutral
$H_2O + SiH^+ \rightarrow Si^+ + H_3O^+$	Ion-neutral
$H^+ + H_2O \rightarrow H_2O^+ + H$	Charge exchange
$He^+ + H_2O \rightarrow H_2O^+ + He$	Charge exchange
$H_2O + h\nu \rightarrow OH + H$	Photodissociation
$H_2O + h\nu \rightarrow H_2O^+ + e^-$	Photoionization
$H_2O + dust \rightarrow H_2O_{ice}$	Adsorption
$Ne^+ + H_2O \rightarrow NeH_2O^+$	Charge exchange

Table 6.1: Main reaction channels relevant for water in de standard disk model, more details can be found in Antonellini et al. (2015).

Parameter	<i>a</i>	<i>b</i>	<i>c</i>	<i>d</i>	<i>e</i>	<i>rm</i> [AU]	$\alpha$
<i>d/g</i> = 100.0	-3.82348609	23.11052247	-2.03604978e-03	1.32424964e+01	0.84197027	0.414	3
<i>d/g</i> = 10.0	-3.44626926	23.05071653	-2.51579966e-03	1.38184098e+01	0.80250736	0.457	3
<i>d/g</i> = 1.0	-3.36225146	23.03655801	-1.90845333e-03	1.39770780e+01	0.81513647	0.465	3
<i>d/g</i> = 0.1	-4.04109527	23.14756948	-1.56425268e-03	1.43917426e+01	1.02804208	0.466	3
<i>d/g</i> = <b>0.01</b>	-3.76117232	23.10188360	-7.38587370e-03	1.56690741e+01	0.98086113	0.470	3
<i>d/g</i> = 0.001	-3.61167711	23.02112424	-9.65443233e-03	1.64581942e+01	1.23648414	0.455	3
$\alpha_{set}=0.1$	-3.65738486	23.08171861	-7.98880413e-03	1.56866851e+01	0.99604788	0.473	3
$\alpha_{set}=\mathbf{0.05}$	-3.44360302	23.05125699	-7.38679484e-03	1.56688955e+01	0.98339369	0.484	3
$\alpha_{set}=0.01$	-3.70449969	23.08926944	-5.86421337e-03	1.56375160e+01	0.99652828	0.470	3
$\alpha_{set}=0.001$	-3.48790069	23.05195284	-6.06411906e-03	1.57158479e+01	0.93850979	0.457	3
$\alpha_{set}=0.0001$	-4.22406505	23.16419110	-4.84510736e-04	1.58435029e+01	0.99373867	0.414	3
$\alpha_{set}=0.00001$	-4.06204780	23.12839652	1.26492090e-03	1.63591046e+01	0.84907205	0.363	3
$\beta = 0.8$	-1.34011742	22.65008904	5.37879388e-03	1.37185914e+01	1.60307585	1.099	2
$\beta = 0.85$	-1.70822869	22.77088797	5.24019604e-03	1.38753868e+01	1.29241951	0.907	2
$\beta = 0.9$	-2.08007760	22.85553472	5.16400118e-03	1.40103447e+01	1.10286071	0.753	2
$\beta = 0.95$	-2.50486344	22.92806366	4.72809529e-03	1.41971629e+01	0.97701864	0.648	2
$\beta = 1.0$	-2.81428564	22.97076138	3.69371009e-03	1.44606303e+01	0.86852380	0.566	2
$\beta = 1.05$	-2.77036634	22.96407768	-8.20943387e-04	1.50821315e+01	0.85420786	0.579	1.5
$\beta = 1.1$	-2.81628793	22.96361090	-7.72539740e-03	1.56293154e+01	0.89302058	0.597	1.5
$\beta = \mathbf{1.15}$	-2.69763372	22.94332596	-8.82712980e-03	1.58347089e+01	1.00653768	0.629	1.5
$\beta = 1.2$	-2.85382579	22.97000349	-1.01654253e-02	1.60474428e+01	1.27466614	0.653	1.5
$\beta = 1.25$	-2.45806599	22.90291040	-1.09369522e-02	1.61204828e+01	1.65403574	0.791	1.5
$a_{max} = 250 \mu m$	-3.30047130	23.02992879	-6.18700541e-03	1.53144906e+01	1.00651970	0.498	3
$a_{max} = 400 \mu m$	-3.29844041	23.02930321	-6.79145396e-03	1.54406704e+01	0.99772737	0.499	3
$a_{max} = 500 \mu m$	-3.29277328	23.02818208	-7.05241910e-03	1.55022210e+01	0.99380805	0.501	3
$a_{max} = 700 \mu m$	-3.27134783	23.02449819	-7.30901039e-03	1.55888782e+01	0.98973283	0.506	3
$a_{max} = \mathbf{1000 \mu m}$	-3.44363066	23.05125738	-7.38653526e-03	1.56688842e+01	0.98339963	0.484	3
$a_{max} = 2000 \mu m$	-3.27016438	23.02278960	-7.56786020e-03	1.58198720e+01	0.97657664	0.507	3
$a_{max} = 5000 \mu m$	-3.27428404	23.02103454	-7.90191548e-03	1.59974941e+01	0.99247625	0.508	3
$a_{max} = 10000 \mu m$	-3.27625023	23.01829228	-8.12249989e-03	1.61213277e+01	1.01788867	0.508	3
$a_{max} = 100000 \mu m$	-3.48101281	23.02652848	-8.30337117e-03	1.64178954e+01	1.23475575	0.483	3
$\alpha_{pow} = 2.0$	-3.44958676	22.83847473	-2.85256487e-03	1.66301042e+01	0.96647945	0.516	1.5
$\alpha_{pow} = 2.5$	-3.65291810	22.93528072	-3.96856094e-03	1.65784946e+01	0.99985174	0.518	1.5
$\alpha_{pow} = 3.0$	-3.21217123	22.96922823	-5.85442124e-03	1.65356353e+01	0.97404003	0.526	1.5
$\alpha_{pow} = \mathbf{3.5}$	-3.44363066	23.05125738	-8.91062663e-03	1.59694624e+01	0.94071980	0.484	1.5
$\alpha_{pow} = 4.0$	-3.18657542	23.00853144	-4.04256936e-03	1.46664825e+01	1.12487021	0.516	1.5
$\alpha_{pow} = 4.5$	-3.04986009	22.97172414	-3.83689368e-03	1.43813049e+01	1.05174471	0.522	1.5
$\xi_{ISM} = 0.5 G_0$	-3.16302525	23.00685665	-6.96450886e-03	1.57539096e+01	0.97404657	0.526	2
$\xi_{ISM} = \mathbf{1 G_0}$	-3.24036901	23.01916189	-7.93379477e-03	1.57761538e+01	0.96908480	0.512	2
$\xi_{ISM} = 10 G_0$	-3.24630345	23.02011051	-1.20875847e-02	1.58677759e+01	0.95686736	0.511	2
$\xi_{ISM} = 100 G_0$	-3.24630345	23.02011051	-1.20875847e-02	1.58677759e+01	0.95686736	0.511	2
$\xi_{ISM} = 10^3 G_0$	-3.25966340	23.02219341	-1.23265769e-02	1.60412109e+01	0.93297108	0.509	2
$\xi_{ISM} = 10^4 G_0$	-3.25578639	23.02156280	-1.13683707e-02	1.62093258e+01	0.91072091	0.509	2
$\xi_{ISM} = 10^5 G_0$	-3.26516495	23.02303698	-1.46266839e-02	1.65710212e+01	0.87494119	0.508	2
$\xi_{ISM} = 10^6 G_0$	-3.27205018	23.02405817	-0.0391374	17.56368485	0.83677659	0.507	2
$f_{PAH} = 1.0$	-3.47326822	23.05168115	-5.39580446e-03	1.56714748e+01	1.01196455	0.516	3
$f_{PAH} = 0.1$	-3.39397357	23.04175353	-6.61038720e-03	1.56748178e+01	0.99814596	0.514	3
$f_{PAH} = \mathbf{0.01}$	-3.44363066	23.05125738	-7.38653526e-03	1.56688842e+01	0.98339963	0.484	3
$f_{PAH} = 0.001$	-4.72967065	23.27130975	-7.43994864e-03	1.56316028e+01	1.09389295	0.609	3
$f_{PAH} = 0.0001$	-4.92224825	23.30059027	-7.48242237e-03	1.56316865e+01	1.09659938	0.605	3
$M_{gas} = 0.1 M_\odot$	-3.40429827	24.05465167	-6.36055789e-03	1.67693706e+01	1.06941638	0.616	2
$M_{gas} = 0.05 M_\odot$	-3.17510887	23.71438612	-7.36353989e-03	1.64700670e+01	1.02902685	0.716	2
$M_{gas} = \mathbf{0.01 M_\odot}$	-3.23984690	23.01907859	-7.93383411e-03	1.57761561e+01	0.96909946	0.571	2
$M_{gas} = 0.001 M_\odot$	-3.54967924	22.05223975	-4.69234081e-03	1.44348283e+01	1.07586536	0.513	2
$M_{gas} = 0.0001 M_\odot$	-3.22794551	20.96573658	-8.33481924e-03	1.36310382e+01	1.14722687	0.462	2
$M_{gas} = 0.00001 M_\odot$	-9.85040876	20.54877163	-1.22594171e-02	1.33780647e+01	0.56402338	0.428	2

Table 6.2: Found parameters for fit by changing a single physical parameter at a time, bold values are the values the values of the reference model. Also *rm* and  $\alpha$  are shown in this table.

$J_{Ka Kc}$	$v_1$	$v_2$	$v_3$	Ortho/Para	$\lambda[\mu\text{m}]$	$E_u[\text{K}]$	$A_{ul} [1/\text{s}]$	$N_{cr}[\text{cm}^{-2}]$	$F [W/\text{cm}^2]$
12 <sub>58</sub>	0	0	0	o	1.710254E+01	3.274E+03	3.705E+00	4.229E+13	3.3916e-19
11 <sub>29</sub>	0	0	0						
13 <sub>130</sub>	0	0	0	o	1.711730E+01	6.259E+03	1.070E+02	1.470E+12	1.1936e-19
12 <sub>121</sub>	0	0	0						
9 <sub>64</sub>	0	0	0	p	1.720910E+01	2.347E+03	3.389E-01	4.413E+14	2.6608e-19
8 <sub>35</sub>	0	0	0						
12 <sub>39</sub>	0	0	0	p	1.721965E+01	3.030E+03	2.557E+00	6.003E+13	2.8718e-19
11 <sub>210</sub>	0	0	0						
11 <sub>39</sub>	0	0	0	p	1.722545E+01	2.439E+03	9.619E-01	1.582E+14	3.4028e-19
10 <sub>010</sub>	0	0	0						
15 <sub>96</sub>	0	0	0	o	1.722848E+01	5.820E+03	5.209E+01	2.992E+12	1.3092e-19
14 <sub>87</sub>	0	0	0						
11 <sub>29</sub>	0	0	0	o	1.735766E+01	2.432E+03	9.493E-01	1.567E+14	4.3530e-19
10 <sub>110</sub>	0	0	0						
13 <sub>122</sub>	0	0	0	p	1.737392E+01	5.882E+03	9.070E+01	1.658E+12	1.4479e-19
12 <sub>111</sub>	0	0	0						
14 <sub>104</sub>	0	0	0	p	1.740491E+01	5.643E+03	6.364E+01	2.364E+12	1.0388e-19
13 <sub>95</sub>	0	0	0						
14 <sub>105</sub>	0	0	0	o	1.740501E+01	5.643E+03	6.361E+01	2.365E+12	1.5465e-19
13 <sub>94</sub>	0	0	0						
9 <sub>46</sub>	0	0	0	p	2.377133E+01	1.929E+03	2.604E-02	2.435E+15	1.0205e-19
9 <sub>19</sub>	0	0	0						
8 <sub>36</sub>	0	0	0	o	2.381676E+01	1.448E+03	6.065E-01	9.173E+13	6.4253e-19
7 <sub>07</sub>	0	0	0						
9 <sub>81</sub>	0	0	0	o	2.385980E+01	2.892E+03	3.128E+01	1.794E+12	5.4794e-19
8 <sub>72</sub>	0	0	0						
9 <sub>82</sub>	0	0	0	p	2.385984E+01	2.892E+03	3.128E+01	1.794E+12	3.6123e-19
8 <sub>71</sub>	0	0	0						
8 <sub>45</sub>	0	0	0	o	2.389518E+01	1.615E+03	1.034E+00	5.328E+13	6.1523e-19
7 <sub>16</sub>	0	0	0						
11 <sub>66</sub>	0	0	0	p	2.392961E+01	3.083E+03	1.612E+01	3.521E+12	2.5811e-19
10 <sub>55</sub>	0	0	0						
11 <sub>56</sub>	0	0	0	o	2.394296E+01	2.876E+03	9.754E+00	5.810E+12	3.6883e-19
10 <sub>47</sub>	0	0	0						
8 <sub>53</sub>	0	0	0	p	3.047223E+01	1.807E+03	8.923E+00	2.977E+12	5.0808e-19
7 <sub>44</sub>	0	0	0						
7 <sub>61</sub>	0	0	0	o	3.052542E+01	1.750E+03	1.355E+01	1.916E+12	9.9663e-19
6 <sub>52</sub>	0	0	0						
7 <sub>62</sub>	0	0	0	p	3.052902E+01	1.750E+03	1.355E+01	1.915E+12	6.1714e-19
6 <sub>51</sub>	0	0	0						
8 <sub>54</sub>	0	0	0	o	3.087090E+01	1.806E+03	8.687E+00	2.941E+12	7.6466e-19
7 <sub>43</sub>	0	0	0						
6 <sub>34</sub>	0	0	0	o	3.089941E+01	9.337E+02	3.504E-01	6.973E+13	7.2798e-19
5 <sub>05</sub>	0	0	0						
8 <sub>18</sub>	0	0	0	o	6.332355E+01	1.071E+03	1.730E+00	1.711E+12	3.8178e-19
7 <sub>07</sub>	0	0	0						
8 <sub>08</sub>	0	0	0	p	6.345802E+01	1.071E+03	1.718E+00	1.712E+12	2.4363e-19
7 <sub>17</sub>	0	0	0						
2 <sub>12</sub>	0	0	0	o	1.795267E+02	1.144E+02	5.617E-02	1.573E+12	6.8456e-19
1 <sub>01</sub>	0	0	0						
2 <sub>21</sub>	0	0	0	o	1.804883E+02	1.941E+02	3.080E-02	4.704E+12	1.9665e-19
2 <sub>12</sub>	0	0	0						
1 <sub>11</sub>	0	0	0	p	2.692723E+02	5.343E+01	1.852E-02	7.853E+11	6.6587e-19
0 <sub>00</sub>	0	0	0						

Table 6.3: Line fluxes of the  $a_{max} = 250\mu\text{m}$  model for the specific regimes; the quantum numbers are indicated for the upper and lower levels (where J is the total angular momentum,  $J = N + S$ , where N is the rotational angular momentum and S the spin, Ka is the projection of N on to the a inertial axis and Kc is the projection of N on to the c inertial axis of the water molecule, the vibrational levels are denoted by  $v_i$  and when i increases a higher level is denoted, also note that  $Ka + Kc$  is odd or even denotes a ortho or para line respectively due to symmetric reasons), whether the transition comes from the ortho or para water species, the wavelength, the energy between the levels, the Einstein A coefficient (for spontaneous emission), the critical density (when the collisional excitation rate equals the radiative decay) and the flux from the specific model are shown for each line from left to right.

Parameter	30.8/17.22	269.2/17.22	179.5/17.22	63.3/17.22	17.22[W/cm <sup>2</sup> ]
d/g = 100.0	30.8312212	58.46774194	135.5011521	36.4855991	1.7360e-21
d/g = 10.0	21.9023726	42.08534291	57.65296191	15.1495555	4.6237e-21
d/g = 1.0	6.66515504	18.73646619	15.88288646	3.53024205	1.7641e-20
d/g = 0.1	3.99615704	6.79744153	5.75747207	2.01610887	7.5983e-20
d/g = 0.01	1.83325856	1.17211039	1.37838816	0.92030506	6.9101e-19
d/g = 0.001	1.62265431	0.45633044	0.83804415	0.88628316	4.7161e-18
$\alpha_{set}=0.1$	1.82630022	1.03844767	1.19935079	0.91283272	6.9315e-19
$\alpha_{set}=0.05$	1.82481227	1.16431222	1.36924936	0.91534079	6.9514e-19
$\alpha_{set}=0.01$	1.82372592	1.46378563	1.93915701	0.93052811	7.0345e-19
$\alpha_{set}=0.001$	1.8445008	1.54831821	2.26388147	1.0148425	7.4920e-19
$\alpha_{set}=0.0001$	1.87574813	1.12519007	1.76931123	1.09434817	9.2731e-19
$\alpha_{set}=0.00001$	1.91402299	1.16958949	1.86935961	1.32059113	1.5225e-18
$\beta=0.8$	0.74453078	0.10728033	0.03793505	0.23860928	2.5095e-19
$\beta=0.85$	0.83395819	0.15719788	0.05479945	0.28448462	1.9471e-19
$\beta=0.9$	0.83395819	0.15719788	0.05479945	0.28448462	1.9471e-19
$\beta=0.95$	0.87985426	0.21516926	0.11332442	0.32194908	2.1682e-19
$\beta=1.0$	0.90284342	0.26070973	0.18138645	0.32117563	2.6658e-19
$\beta=1.05$	1.1069411	0.45816321	0.44121595	0.44487947	3.5758e-19
$\beta=1.1$	1.53410469	0.69276953	0.79873164	0.72314666	5.0301e-19
$\beta=1.15$	2.04316948	0.81260270	1.05364155	1.03988302	7.1810e-19
$\beta=1.2$	2.51576115	0.83535116	1.21180179	1.33407622	9.9612e-19
$\beta=1.25$	3.10663616	0.78520214	1.27864226	1.65583524	1.3110e-18
$a_{max}=250$	2.24714941	1.95682967	2.01172564	1.12195839	3.4028e-19
$a_{max}=400$	2.08217525	1.63406259	1.75291743	1.04266524	4.3103e-19
$a_{max}=500$	2.01442724	1.49836945	1.64078431	1.01420021	4.8450e-19
$a_{max}=700$	1.92799514	1.32495879	1.50139672	0.96769324	5.7635e-19
$a_{max}=1000$	1.82481227	1.16431222	1.36924936	0.91534079	6.9514e-19
$a_{max}=2000$	1.67605789	0.92595494	1.17194484	0.8442362	9.9561e-19
$a_{max}=5000$	1.511870	0.7139774	0.99346198	0.76101308	1.5754e-18
$a_{max}=10000$	1.43818438	0.60143578	0.89654232	0.73310918	2.2009e-18
$a_{max}=100000$	1.62836145	0.45096553	0.83176448	0.89778255	4.7487e-18
$\alpha_{pow}=2.0$	2.82267984	0.31449870	0.65687663	1.52171077	1.0732e-17
$\alpha_{pow}=2.5$	3.01800607	0.37587810	0.81629428	1.72124624	8.6693e-18
$\alpha_{pow}=3.0$	2.28188632	0.47535936	0.90880523	1.2282311	4.7097e-18
$\alpha_{pow}=3.5$	1.82481227	1.16431222	1.36924936	0.91534079	6.9514e-19
$\alpha_{pow}=4.0$	2.41290727	5.10491507	5.12134503	1.21943748	1.4364e-19
$\alpha_{pow}=4.5$	1.66758225	4.37904988	4.60016231	0.86297522	1.6019e-19
$\xi_{ISM}=0.5 G_0$	1.82224329	1.14916968	1.37232086	0.91380796	6.9612e-19
$\xi_{ISM}=1 G_0$	1.82323697	1.16341456	1.36828266	0.91447784	6.9596e-19
$\xi_{ISM}=10 G_0$	1.82785203	1.34141055	1.51361594	0.91831871	6.9661e-19
$\xi_{ISM}=100 G_0$	1.85385288	2.24723771	4.18449677	1.00537411	6.9779e-19
$\xi_{ISM}=10^3 G_0$	5.49148466	9.07715540	50.9060656	19.6398109	7.1518e-19
$\xi_{ISM}=10^4 G_0$	56.1692394	1.17402968	12.4618277	66.7461049	8.3503e-18
$\xi_{ISM}=10^5 G_0$	37.6095485	0.04986302	0.65255004	17.8003857	1.5039e-16
$\xi_{ISM}=10^6 G_0$	29.6682448	0.02909562	0.33138542	10.0739538	2.8937e-16
$f_{PAH}=1.0$	6.37366482	2.03484304	2.68144503	4.08286301	8.5756e-19
$f_{PAH}=0.1$	2.58565721	1.50369264	1.73991417	1.40145553	7.4337e-19
$f_{PAH}=0.01$	1.82481227	1.16431222	1.36924936	0.91534079	6.9514e-19
$f_{PAH}=0.001$	1.73766362	1.08240183	1.29323526	0.86222924	6.9064e-19
$f_{PAH}=0.0001$	1.73207273	1.07467636	1.28599273	0.85937455	6.875e-19
$M_{gas}=0.1 M_\odot$	1.93228856	0.61425097	1.212621	1.07357418	6.2087e-18
$M_{gas}=0.05 M_\odot$	1.52423297	0.60533021	1.01705668	0.81531461	3.8460e-18
$M_{gas}=0.01 M_\odot$	1.82323697	1.16341456	1.36829703	0.91447784	6.9596e-19
$M_{gas}=0.001 M_\odot$	2.90305124	3.4382328	3.23120898	1.46470743	7.2069e-20
$M_{gas}=0.0001 M_\odot$	3.13922750	2.49913596	3.21199383	1.73135304	2.1411e-20
$M_{gas}=0.00001 M_\odot$	7.97550351	2.25515567	5.55719866	4.30376288	6.2213e-21

Table 6.4: Calculated line ratios of specific water emission lines and flux of the 17.22  $\mu\text{m}$  line for all the different models.



# Bibliography

[1] *The National Radio Astronomy Observatory (NRAO), Credit: C. Brogan, B. Saxton (NRAO/AUI/NSF); ALMA (NRAO/ESO/NAOJ)*, ALMA image of the young star HL Tau and its protoplanetary disk. This best image ever of planet formation reveals multiple rings and gaps that herald the presence of emerging planets as they sweep their orbits clear of dust and gas.

<https://public.nrao.edu/static/pr/planet-formation-alma.html>

[2] *European Southern Observatory (ESO), Credit: B. Saxton (NRAO/AUI/NSF); ALMA (ESO/NAOJ/NRA)*, This beautiful image, captured with the Atacama Large Millimeter/submillimeter Array (ALMA) features a protoplanetary disc surrounding the young star Elias 2-27, some 450 light years away. ALMA has discovered and observed plenty of protoplanetary discs, but this disc is special as it shows two distinct spiral arms, almost like a tiny version of a spiral galaxy. Previously, astronomers noted compelling spiral features on the surfaces of protoplanetary disks, but it was unknown if these same spiral patterns also emerged deep within the disc where planet formation takes place. ALMA, for the first time, was able to peer deep into the mid-plane of a disk and discovered the clear signature of spiral density waves. Nearest to the star, ALMA found a flat disc of dust, which extends to what would approximately be the orbit of Neptune in our own Solar System. Beyond that point, in the region analogous to our Kuiper Belt, ALMA detected a narrow band with significantly less dust, which may be an indication for planet in formation. Springing from the outer edge of this gap are the two sweeping spiral arms that extend more than 10 billion kilometers away from their host star. The discovery of spiral waves at these extreme distances may have implications on the theory of planet formation.

<https://www.eso.org/public/images/potw1640a>

- [3] K.Zhang, K.M.Pontoppidan, C.Salyk and G.A.Blake, *Evidence for a Snow Line beyond the Transitional Radius in the TW Hya Protoplanetary Disk. The Astrophysical Journal*, 766:82(12pp), 2013 April 1
- [4] S.Antonellini, I.Kamp, P.Riviere-Marichalar, R.Meijerink, P.Woitke, W.-F.Thi, M.Spaans, G.Aresu and G.Lee, *Understanding the water emission in the mid- and far-IR from protoplanetary disks around T Tauri stars. Astronomy & Astrophysics*, 582 A105, 2015 July 19
- [5] B.Siemer, S.Roling, R.Frigge, T.Hoger, R.Mitznera and H.Zacharias, *Free-electron laser induced processes in thin molecular ice. Faraday Discuss*, 2014,168, 553-569, 2013 December 17
- [6] *Earths in Other Solar Systems (EOS)*, Credit: [http : //www.til - birnstiel.de](http://www.til-birnstiel.de), Illustration of a protoplanetary disk surrounding a young star.  
[http : //eos - nexus.org/2016/03/29/dust - grains - frogs - and - the - formation - of - habitable - planets](http://eos-nexus.org/2016/03/29/dust-grains-frogs-and-the-formation-of-habitable-planets)
- [7] *Frederick M. Walter*, A Potpourri of Circumstellar Disks.  
[http : //www.astro.sunysb.edu/fwalter/AST101/cs\\_disks.html](http://www.astro.sunysb.edu/fwalter/AST101/cs_disks.html)
- [8] *Cosmic Dust*, Wikipedia, used on 2017 March 8.  
[https : //en.wikipedia.org/wiki/Cosmic\\_dust](https://en.wikipedia.org/wiki/Cosmic_dust)
- [9] *Polycyclic aromatic hydrocarbon*, Wikipedia, used on 2017 March 6.  
[https : //en.wikipedia.org/wiki/Polycyclic\\_aromatic\\_hydrocarbon](https://en.wikipedia.org/wiki/Polycyclic_aromatic_hydrocarbon)
- [10] *Water structure and science*, last updated by Martin Chaplin 2016 October 6.  
[http : //www1.lsbu.ac.uk/water/ortho\\_para\\_water.html](http://www1.lsbu.ac.uk/water/ortho_para_water.html)
- [11] *Water structure and science*, Electrical detection of orthopara conversion in fullerene-encapsulated water,Nature Communications 6:8112, August 2015.  
[https : //www.researchgate.net/publication/281236187\\_Electrical\\_detection\\_of\\_ortho - para\\_conversion\\_in\\_fullerene - encapsulated\\_water](https://www.researchgate.net/publication/281236187_Electrical_detection_of_ortho-para_conversion_in_fullerene-encapsulated_water)

